Monthly Notices of the ROYAL ASTRONOMICAL SOCIETY

MNRAS **467,** 597–618 (2017)
Advance Access publication 2017 January 13

doi:10.1093/mnras/stx084

The remarkable outburst of the highly evolved post-period-minimum dwarf nova SSS J122221.7−311525⋆

V. V. Neustroev,[1,2]† T. R. Marsh,[3] S. V. Zharikov,[4] C. Knigge,[5] E. Kuulkers,[6] J. P. Osborne,[7] K. L. Page,[7] D. Steeghs,[3] V. F. Suleimanov,[8] G. Tovmassian,[4] E. Breedt,[3] A. Frebel,[9] Ma. T. García-Díaz,[4] F.-J. Hambsch,[10,11] H. Jacobson,[9] S. G. Parsons,[12] T. Ryu,[13,14] L. Sabin,[4] G. Sjoberg,[11,15] A. S. Miroshnichenko,[16] D. E. Reichart,[17] J. B. Haislip,[17] K. M. Ivarsen,[17] A. P. LaCluyze[17] and J. P. Moore[17]

[1]*Finnish Centre for Astronomy with ESO (FINCA), University of Turku, Väisäläntie 20, FI-21500 Piikkiö, Finland*
[2]*Astronomy research unit, PO Box 3000, FI-90014 University of Oulu, Finland*
[3]*Department of Physics, University of Warwick, Gibbet Hill Road, Coventry CV4 7AL, UK*
[4]*Instituto de Astronomia, Universidad Nacional Autonoma de Mexico, Apdo. Postal 877, Ensenada, Baja California, 22800 Mexico*
[5]*School of Physics and Astronomy, University of Southampton, Southampton SO17 1BJ, UK*
[6]*European Space Astronomy Centre (ESA/ESAC), Science Operations Department, 28691 Villanueva de la Cañada, Madrid, Spain*
[7]*Department of Physics & Astronomy, University of Leicester, University Rd, Leicester LE1 7RH, UK*
[8]*Institut für Astronomie und Astrophysik, Universität Tübingen, Sand 1, D-72076 Tübingen, Germany*
[9]*Department of Physics and Kavli Institute for Astrophysics and Space Research, Massachusetts Institute of Technology, Cambridge, MA 02139, USA*
[10]*Vereniging voor Sterrenkunde, Oude Bleken 12, B-2400 Mol, Belgium*
[11]*American Association of Variable Star Observers, 49 Bay State Road, Cambridge, MA 02138, USA*
[12]*Departmento de Física y Astronomía, Universidad de Valparaíso, Avenida Gran Bretana 1111, Valparaíso, 2360102, Chile*
[13]*SOKENDAI, The Graduate University for Advanced Studies, 2-21-1 Osawa, Mitaka, Tokyo 181-8588, Japan*
[14]*National Astronomical Observatory of Japan, 2-21-1 Osawa, Mitaka, Tokyo 181-8588, Japan*
[15]*The George-Elma Observatory, New Mexico Skies, 9 Contentment Crest, #182, Mayhill, NM 88339, USA*
[16]*University of North Carolina at Greensboro, Greensboro, NC 27402, USA*
[17]*Department of Physics and Astronomy, University of North Carolina, Chapel Hill, NC 27599, USA*

Accepted 2017 January 11. Received 2016 December 23; in original form 2016 May 29

ABSTRACT

We report extensive 3-yr multiwavelength observations of the WZ Sge-type dwarf nova SSS J122221.7−311525 during its unusual double superoutburst, the following decline and in quiescence. The second segment of the superoutburst had a long duration of 33 d and a very gentle decline with a rate of 0.02 mag d^{-1}, and it displayed an extended post-outburst decline lasting at least 500 d. Simultaneously with the start of the rapid fading from the superoutburst plateau, the system showed the appearance of a strong near-infrared excess resulting in very red colours, which reached extreme values ($B - I \simeq 1.4$) about 20 d later. The colours then became bluer again, but it took at least 250 d to acquire a stable level. Superhumps were clearly visible in the light curve from our very first time-resolved observations until at least 420 d after the rapid fading from the superoutburst. The spectroscopic and photometric data revealed an orbital period of 109.80 min and a fractional superhump period excess $\lesssim$0.8 per cent, indicating a very low mass ratio $q \lesssim 0.045$. With such a small mass ratio the donor mass should be below the hydrogen-burning minimum mass limit. The observed infrared flux in quiescence is indeed much lower than is expected from a cataclysmic variable with a near-main-sequence donor star. This strongly suggests a brown-dwarf-like nature for the donor and that SSS J122221.7−311525 has already evolved away from the period minimum towards longer periods, with the donor now extremely dim.

Key words: binaries: close – stars: evolution – stars: individual: SSS J122221.7−311525 – novae, cataclysmic variables.

⋆This paper includes data gathered with the 6.5 m Magellan Telescopes located at Las Campanas Observatory, Chile.

†E-mail: vitaly@neustroev.net

1 INTRODUCTION

In the accreting white dwarf (WD) systems known as cataclysmic variable stars (CVs – for a comprehensive review, see Warner 1995), accretion is the dominant factor in their discovery through line emission and outbursts. The donor components in CVs are low-mass main-sequence stars or brown dwarfs which lose matter via the inner Lagrangian point. In the absence of a strong magnetic field, the material transferred from the donor star forms an accretion disc around the WD. Dwarf novae are an important subset of CVs with relatively low mass-transfer rates, the discs of which can suffer thermal instabilities, resulting in outbursts for which CVs are named (for review of the disc-instability model see e.g. Cannizzo 1993; Osaki 1996; Lasota 2001). The recurrence time of the outbursts is usually weeks or a few months and their amplitude is mostly less than 6 mag. However, the outbursts in different dwarf novae have different amplitudes, light-curve shapes, durations and recurrence times. Based on the variety of these parameters, a few sub-types have been assigned to the dwarf nova class.

SU UMa-type dwarf novae have short orbital periods, usually below the 2–3 h CV period gap, and show two types of outbursts: short (normal) outbursts lasting a few days, and less frequent superoutbursts which have a slightly larger amplitude and a longer duration of about two weeks. At the short period end of the CV orbital period distribution, accretion rates are low, and some systems only outburst once every several years or even decades. Such systems compose an extreme subgroup of the SU UMa-type dwarf novae, called WZ Sge-type stars (for a modern and comprehensive review of the WZ Sge-type objects, see Kato 2015). Their other peculiar properties are very large superoutburst amplitudes exceeding 6 mag and the lack or great rarity of normal outbursts.

A unique property of superoutbursts is the appearance of superhumps, low-amplitude modulations with a period of a few per cent longer than the orbital one. The superhump phenomenon is well explained by the tidal instability of the accretion disc (Vogt 1982; Whitehurst 1988; Osaki 1989). This instability grows when a disc expands beyond the 3:1 resonance radius that causes the disc to become quasi-elliptical and precess, initiating superhumps. The period of superhumps $P_{\rm sh}$ is known to depend on the orbital period $P_{\rm orb}$ and the mass ratio $q = M_2/M_{\rm wd}$, where M_2 and $M_{\rm wd}$ are the masses of the donor and WD, respectively. An empirical $P_{\rm sh}$–q relation (see e.g. Patterson et al. 2005) is an important tool to estimate q without the recourse to spectroscopy. In particular, it was shown that the distribution of the mass ratios of the donor and WD in WZ Sge-type stars shows a sharp peak between 0.07 and 0.08 (Kato 2015).

The CVs with such small mass ratios are of a special interest because a significant number of 'period bouncers' should be present among them. According to standard evolutionary theory, CVs evolve from longer to shorter orbital periods until a minimum period is reached (≈80 min), when the donor star becomes of a substellar mass and partially degenerate, resulting in a kind of a brown-dwarf-like object. Systems that have passed beyond $P_{\rm min}$ are evolving back towards longer periods (see Kolb 1993; Howell, Rappaport & Politano 1997; Gänsicke et al. 2009; Knigge, Baraffe & Patterson 2011, and references therein). This has long been predicted to be the 'graveyard' and current state of 70 per cent of all CVs (Kolb 1993), however only about a dozen more or less robust candidates for such period bouncer systems have been identified until now, out of about 1000 of known CVs (for a fairly recent compilation see Patterson 2011).

One such system, called SSS J122221.7−311525[1] (hereafter SSS J122222), was discovered on 2013 January 1 at $V = 12.3$ by the Catalina Real Time Survey (CRTS; Drake et al. 2013), and was subsequently found to have been in outburst by 2012 December 16 (with unfiltered CCD magnitude 11.8; Levato et al. 2013). The large outburst amplitude (the average quiescent magnitude of the counterpart was found to be ≈19; Drake et al. 2013), the appearance of its optical spectrum (Marsh et al. 2013) and the detection of an 'S-wave' sinusoidal component in the emission lines with a period of about 80 to 95 min allowed Kuulkers et al. (2013) to propose the WZ Sge-type dwarf nova classification for SSS J122222. Kato et al. (2013) discussed some of the outburst properties of SSS J122222, studied the superhump period changes in the system and found that SSS J122222 has a very small mass ratio, $q < 0.05$. They also concluded that the relatively long orbital period $P_{\rm orb}$ (which was not known, but should be close to the average superhump period of ∼111 min) and low q make this object a perfect candidate for a period bouncer. The confirmation of the period bouncer status would be of great importance due to the long orbital period of SSS J122222, which would make this binary the most evolved CV (Knigge et al. 2011).

For more than three years we have been performing extensive X-ray–ultraviolet (UV)–optical–near-infrared (NIR) photometric and spectroscopic observations of SSS J122222. The observations were taken from 2013 January 5 (four days after the discovery) until 2016 April 17, during the superoutburst, the following decline and in quiescence. These data provide crucial insights into the properties of SSS J122222. We found that a number of observed features are quite unusual when compared with other WZ Sge-type systems. Although most of these features are not completely unique, their union in one object makes SSS J122222 a remarkable case of the WZ-Sge-type system. Our unprecedentedly detailed, multiwavelengths observations allow us to shed more light on mechanisms underlying the system's extraordinary properties. In this paper, we concentrate on the long-term evolution of the binary as revealed by the UV–optical–NIR data.

2 OBSERVATIONS

During our observing campaign we used many ground- and space-based telescopes equipped with different instruments. All details on the observations and data reduction can be found in Appendix A. Here we describe shortly the data used in our analysis.

Our optical time-resolved photometric observations started on 2013 January 8, ∼7 d after the discovery announcement by CRTS (Drake et al. 2013). From then on, the observations were conducted almost every clear night until 2013 April 21. After a short interruption, the observations were resumed on 2013 May 4 and continued until 2013 June 18, the end of visibility of the source. Thus, about 100 nights of time-resolved photometric data were taken during this interval. We restarted the observations on 2014 January 13, when the star became visible again, and finished on 2014 June 28. A total of 35 nights of data were obtained during 2014. In the beginning of 2015 we obtained seven additional sets of time-resolved data. In January–April of 2016 we took several single-shot observations. The final observation was taken on 2016 April 17. The observations were taken with a 0.40-m f/6.8 Optimized Dall Kirkham (ODK) telescope of the Remote Observatory Atacama Desert (ROAD) in

[1] Also known as SSS130101:122222−311525, 1RXS J122221.5−311545 and OT J122221.6−311525.

Table 1. The averaged magnitudes of SSS J122222 on 2013 February 5 (the plateau stage of the superoutburst) and on 2016 April 7–17 (quiescence). The superoutburst *U* magnitude is given in the Bessel filter, whereas for the quiescent state we show the *Swift u* magnitude.

State	*uvw2*	*uvm2*	*uvw1*	*u*/*U*	*B*	*V*	R_c	I_c	*J*	*H*	*Ks*
Superoutburst		11.08(5)		11.91(5)	12.65(4)	12.69(3)	12.68(3)	12.77(4)			
Quiescence	17.65(8)	17.53(9)	17.57(7)	17.97(7)	19.05(5)	19.00(5)	18.72(5)	18.76(5)	18.47(5)	18.31(7)	17.77(23)

Chile, a 0.35-m Celestron C14 robotic telescope at New Mexico Skies in Mayhill, New Mexico, two 0.4-m robotic PROMPT telescopes located in Chile (Reichart et al. 2005), and with the 0.84-m telescope at the Observatorio Astronómico Nacional at San Pedro Mártir (OAN SPM) in Mexico. A significant part of our photometric data was taken with Johnson–Cousins $BV(RI)_C$ filters, and other observations were performed with the *V* or *R* filters, or unfiltered. Table A2 provides the journal of these observations.

On 2016 April 7 we conducted a near-infrared observation using the Infrared Survey Facility (IRSF) at Sutherland, South Africa. The IRSF consists of a 1.4 m telescope and Simultaneous Infrared Imager for Unbiased Survey (SIRIUS: Nagayama et al. 2003), which can obtain *J*, *H* and *Ks*-band images simultaneously.

The optical spectroscopic observations of SSS J122222 were performed on 16 nights between 2013 January 5 and 2013 May 5. Additional observations were taken on 2015 May 5, and on 2016 February 9 and 10. The spectra were obtained with the 4.2-m William Herschel Telescope on La Palma, the 2.1-m telescope at the OAN SPM, the 6.5-m Magellan Clay Telescope at Las Campanas Observatory near La Serena in Chile, and with the VLT-UT1 and VLT-UT2 telescopes at Paranal Observatory, Chile. Spectra were obtained in both single-shot and time-resolved manner with different instrumental setups and exposure times. Table A4 provides the journal of the optical spectroscopic observations.

The *Swift* X-ray satellite (Gehrels et al. 2004) started observing SSS J122222 on 2013 January 6, 5.8 d after the discovery announcement (Kuulkers et al. 2013). For each observation, data were collected using both the X-ray Telescope (XRT; Burrows et al. 2005) and the UV/Optical Telescope (UVOT; Roming et al. 2005) with the *uvm2* filter in position. In this paper we present only the UV/Optical part of the observations. The observations were obtained approximately every 1–3 d until 2013 July 1. Two additional observations were performed on 2014 June 26 and 2015 January 16. A final data set was collected on 2016 April 17. This UVOT observation was carried out in all six available filters.

In Section 3.1 we show that SSS J122222 had returned to quiescence in the beginning of 2015. In Table 1 we summarize the averaged magnitudes of SSS J122222 in all the available filters, obtained on 2016 April 7–17 (quiescence) and on 2013 February 5 (the superoutburst).

3 OPTICAL AND UV PHOTOMETRY

3.1 Long-term light curve and the colour evolution

Throughout the paper, we will denote time in units of days since 2013 January 8, when we began our time-resolved photometric observations. Thus, $T = 0$ corresponds to HJD 245 6300.0.

Fig. 1 shows the light curves of SSS J122222 containing all our observations in the optical and UV filters taken over about three years. In the inset of this figure we also show the overall light curve which includes the pre-outburst 1-d averaged data from the Catalina Real-time Transient Survey (CRTS) observations[2] (Drake et al. 2009) begun 10 years ago from 2005 August 5. The pre-outburst data reveal a half-magnitude variability between ∼18.5 and ∼19 mag on few years' time-scale, but show no indication of previous outbursts.

The most notable feature of the superoutburst is its unusual double structure and long duration (Fig. 2). Unfortunately, the first segment of the superoutburst was scarcely observed. The most recent observations prior to the superoutburst were obtained on 2012 August 13 ($T = -147$), when the system was at $V \sim 18.3$. The earliest observations of SSS J122222 in outburst were obtained on $T = -22$ (∼11.8 mag; Levato et al. 2013). Subsequent photometry showed that the object had still been near maximum light until at least $T = -5.8$ ($V = 12.3$; Drake et al. 2013), after that SSS J122222 had faded to magnitude ∼15.5 on $T = -2.4$ and ∼16 on $T = -1.5$. Thus, the duration of the superoutburst's first segment was at least 16 d.

When fading, the transient did not reach its quiescent level, and rebrightened again on $T = 3$, entering the second segment of the superoutburst (Neustroev & Sjoberg 2013). We began our photometric observations on $T = 0$, near the minimum light of this temporary fading stage ($V = 16.8$). During the rise the optical flux increased at a rate of ∼2.8 mag d^{-1}. The outburst's second segment had reached the maximum of $V = 12.2$ on $T = 7$. After a short 'dip' by ∼0.4 mag exhibited during $T = 9$–10, SSS J122222 reached another local maximum of $V = 12.3$ on $T = 13$ and then monotonically faded very slowly. On $T = 37$ we observed a rapid fading with a rate of 1.31 ± 0.01 mag d^{-1}, followed by a slow decline. Thus, the duration of the second segment of the superoutburst was about 33 d. We note that though the peculiar pattern of the light curve of SSS J122222 is not unprecedented and similar double superoutbursts have been seen in a few other CVs (e.g. OT J184228.1+483742, see fig. 1 in Kato et al. 2013) and transient low-mass X-ray binaries (e.g. XTE J1118+480, Kuulkers 2001), yet the superoutburst of SSS J122222 was the longest of any other known dwarf novae. During 33 d of the second segment of the superoutburst SSS J122222 faded by only ∼0.7 mag. The average fading rate during $T = 13$–20 was just 0.006 ± 0.001 mag d^{-1}, after that it increased to 0.032 ± 0.001 mag d^{-1} ($T = 20$–35). Such a slow, gradual decline is atypical for SU UMa stars, whose plateau slope is usually about 0.11 ± 0.01 mag d^{-1} (Warner 1995). See Section 6.1 for further discussion of atypical properties of the light curve.

The shoulder in the beginning of the second segment of the superoutburst resembles a so-called precursor outburst, a normal outburst which is often observed shortly before the superoutburst (Marino & Walker 1979), and which is thought to trigger it (Osaki 1989; Osaki & Kato 2013). We note, however, that in contrast to SSS J122222, the maximum light of precursors is usually lower by 0.5–1 mag than that of the following superoutbursts (see e.g. the very detailed high-fidelity *Kepler* light curves of several superoutbursts of two SU UMa stars; Cannizzo et al. 2012), thus the origin of

[2] http://nesssi.cacr.caltech.edu/DataRelease/

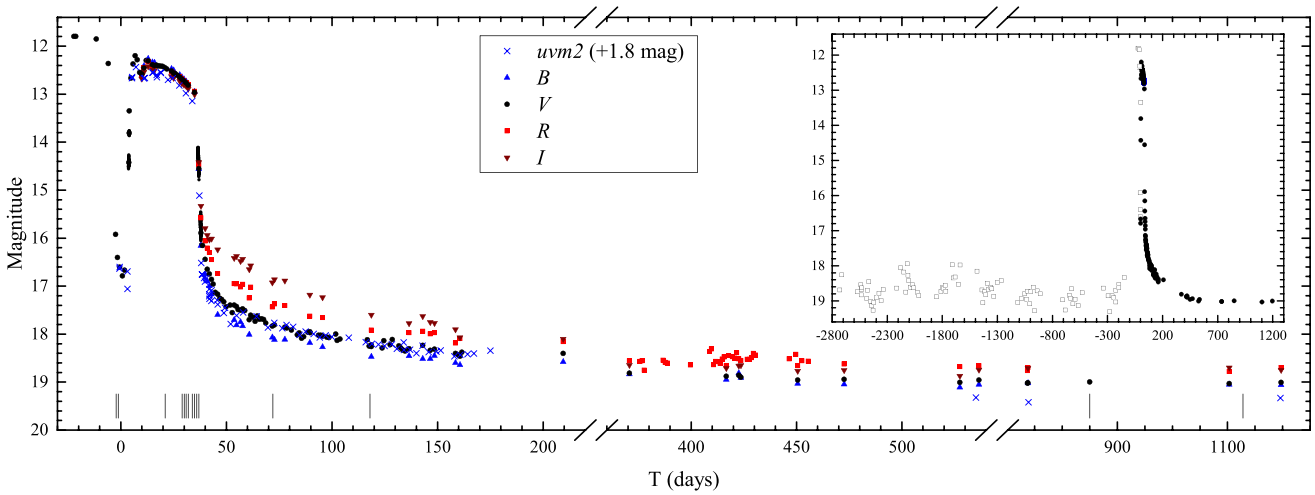

Figure 1. The light curve of the superoutburst of SSS J122222 in all the available optical and UV filters. Each point is the 1-d average of observations in the corresponding filter. Short vertical lines mark epochs of optical spectra. In the inset the overall light curve is shown which includes the pre-outburst 1-d averaged data from the CRTS observations (the open squares). *T* is the number of days elapsed since HJD 245 6300.0.

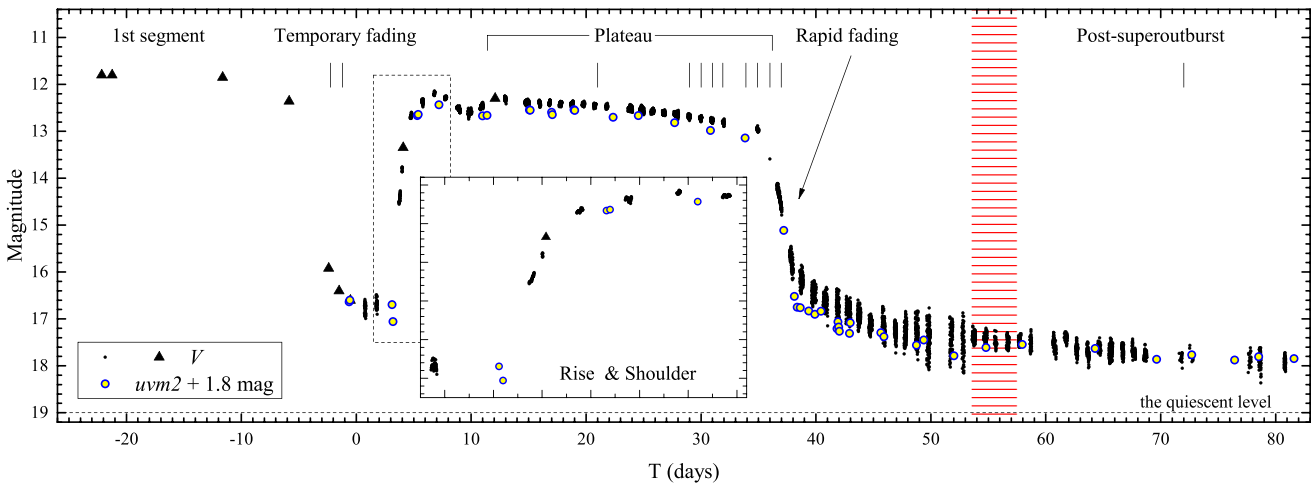

Figure 2. A superoutburst segment of the light curve in the *V* and *uvm*2 filters. Black points are the individual observations in the *V* filter. The triangles represent the optical data taken from the literature and other sources. Blue/yellow symbols are the observations in the *uvm*2 filter, shifted by 1.8 mag for clarity. Short vertical lines mark epochs of optical spectra. The different stages of the superoutburst are indicated. The red vertical ribbon marks the days of the reddest optical spectra. In the inset the rise and the shoulder in the beginning of the second segment of the outburst are shown.

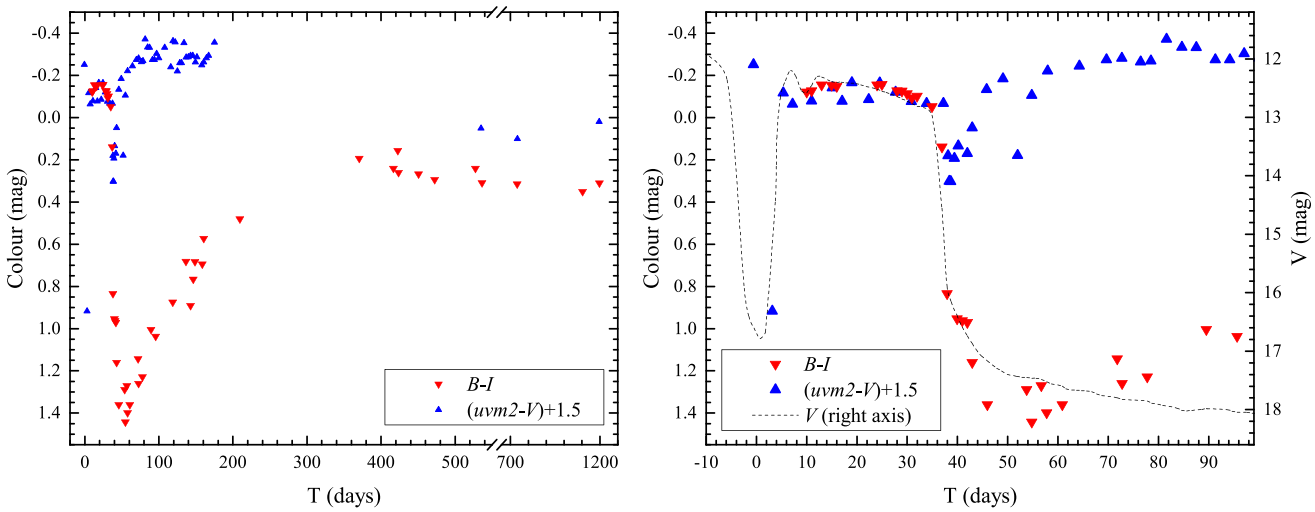

Figure 3. Variations of optical and UV colour indices. Left: the entire period of our observations. Right: a superoutburst segment is shown together with the *V*-band light curve.

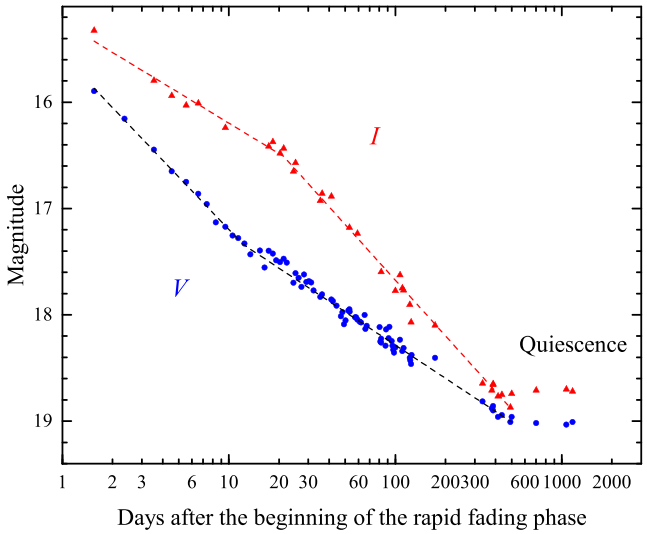

Figure 4. The *V* and *I* photometry during the decline stage of the superoutburst, plotted with a logarithmic time-scale. The days are counted from the beginning of the rapid fading phase at $T = 36.4$.

the shoulder in SSS J122222 might be different from that of the precursors discussed above.

The shapes of the optical and UV light curves are qualitatively similar. In particular, the data do not show any apparent signs of a UV-delay in the early rising phase of the second segment of the superoutburst.[3] Note, however, that at the very beginning of the optical rise the UV flux showed a drop by ∼0.25 mag (see the inset in Fig. 2). We do not have simultaneous optical photometry which would enable us to verify such a behaviour, although the detailed *Kepler* observations of many CV superoutbursts (e.g. Cannizzo et al. 2012) do not seem to show such drops at optical wavelengths. On the other hand, the drops of the UV flux in the beginning of outbursts were reported for several DNe (Wu & Panek 1983; Verbunt 1987). They, however, were different in the sense that they occurred after an initial rise, and after the drop the rise resumed. In SSS J122222 this UV drop occurred before the rise.

Fig. 1 displays an apparent difference in the post-outburst behaviour of the transient in different wavelengths. The magnitude of the decline during the rapid fading phase decreases greatly towards longer wavelengths, resulting in strong colour evolution (Fig. 3). Fig. 4 shows the optical photometry during and after the rapid fading phase, plotted with a logarithmic time-scale. For clarity, we show only the *V* and *I* light curves, but the *B* and *R* look similar. We found that all the light curves are well described by a broken power law as a function of time, with the time origin being at $T = 36.4$ and a slope-break some 20 d later. The power-law indices of the decline are given in Table 2. It is unclear how common is such a (broken) power-law decline among CVs and LMXBs, because we found no papers, either observational or theoretical, reporting on it.

[3] A UV-delay, a lag as long as one day between the rise to outburst in the optical flux and the rise in UV, is observed in some dwarf novae (see Verbunt 1987 and Warner 1995, and references therein), the cause of which is still not fully understood. We note, however, that the observed rise in SSS J122222 had occurred after the temporary fading stage, from the level of about 2 mag brighter than that in quiescence. Thus, it is not clear if the discussion of the existence or non-existence of the UV-delay in such conditions is relevant.

Table 2. The power-law indices (columns 2 and 3) of the broken power-law decline of SSS J122222 in the *B*, *V*, *R* and *I* bands (in flux units), and the number of days (column 4) elapsed between the beginning of the rapid fading phase at $T = 36.4$ and the slope-break.

Band	Before the break	After the break	Break time after $T = 36.4$
B	-0.58 ± 0.03	-0.33 ± 0.01	∼23
V	-0.64 ± 0.01	-0.43 ± 0.01	∼18
R	-0.54 ± 0.02	-0.43 ± 0.02	∼24
I	-0.38 ± 0.03	-0.70 ± 0.01	∼24

From Fig. 4 it is also clearly seen that SSS J122222 has not fully recovered from the outburst even 500 d after the rapid fading phase because it was still fading with the same rate. Only our observations obtained on and after $T = 736$ revealed that the data do not follow the decline trend anymore, confirming that the transient had finally returned to quiescence. The following observations showed nearly constant magnitudes. Thus, the total amplitude of the outburst was ∼7 mag and its post-outburst decline lasted no less than 500 d.

During the superoutburst the colour indices[4] demonstrated dramatic changes with time, and the colour curve has an extraordinary shape (Fig. 3), never observed before in such detail. At the superoutburst plateau the optical colour indices varied slowly around 0, their average values were quite usual for a dwarf nova in outburst (Warner 1995): $B–V = -0.04 \pm 0.01$, $V–R = 0.00 \pm 0.01$, $R–I = -0.09 \pm 0.01$. With the start of the decline, the object had begun reddening. The colour indices reached the extreme values some 20 d later, around the time of the slope-break of the broken power-law decline, at $T \simeq 54$–58: $B–V = 0.32 \pm 0.05$, $V–R = 0.48 \pm 0.03$, $R–I = 0.55 \pm 0.03$. These colours are redder than in most dwarf novae in quiescence (Echevarria 1984; Echevarria & Jones 1984; Kato, Maehara & Uemura 2012). The colours then turned back to becoming bluer. This trend continued for several hundred days. Only the data obtained after $T \sim 472$ revealed nearly stable, relatively blue colours: $B–V = 0.06 \pm 0.05$, $V–R = 0.30 \pm 0.03$, $R–I = -0.07 \pm 0.10$. Although they are not so atypical for WZ Sge-type dwarf novae (Kato et al. 2012), the colours are significantly bluer than in many of them in quiescence (compare e.g. $B–I = 0.43$ in SSS J122222 and $B–I = 0.75$ in V455 And; Neustroev et al. 2013).

The reddening of optical light after the superoutburst has been previously detected in several WZ Sge-type stars (Kato 2015). For example, a similarly strong cool continuum source was reported for EG Cnc by Patterson et al. (1998), which also showed the red colours ($B–I \simeq 1.4$). However, multicolour observations after the active stage of superoutbursts are rare and sporadic, and no detailed study of the above phenomenon has ever been presented.

In contrast to the optical wavelengths, the UV data showed redder colours at the superoutburst plateau, and bluer during the post-outburst stage (Fig. 3). However, the data obtained after the long gap in our observations (after $T \sim 535$) show that in quiescence the *uvm*2-*V* index dropped again to the level even lower than during the plateau, reaching a nearly stable value of -1.44 ± 0.10 mag. We also note three red jumps in the *uvm*2-*V* curve (see the right-hand panel of Fig. 3). Besides the one in the beginning of the rise, mentioned above, another reddening episode had begun immediately after the beginning of the rapid fading phase, almost simultaneously with the optical colours (but possibly after a short delay). However, *uvm*2-*V* reached the maximum value in less than a day and returned to the

[4] In order to calculate the values of the *uvm*2-*V* indices, we interpolated the *V* magnitudes to the times of the UV observations.

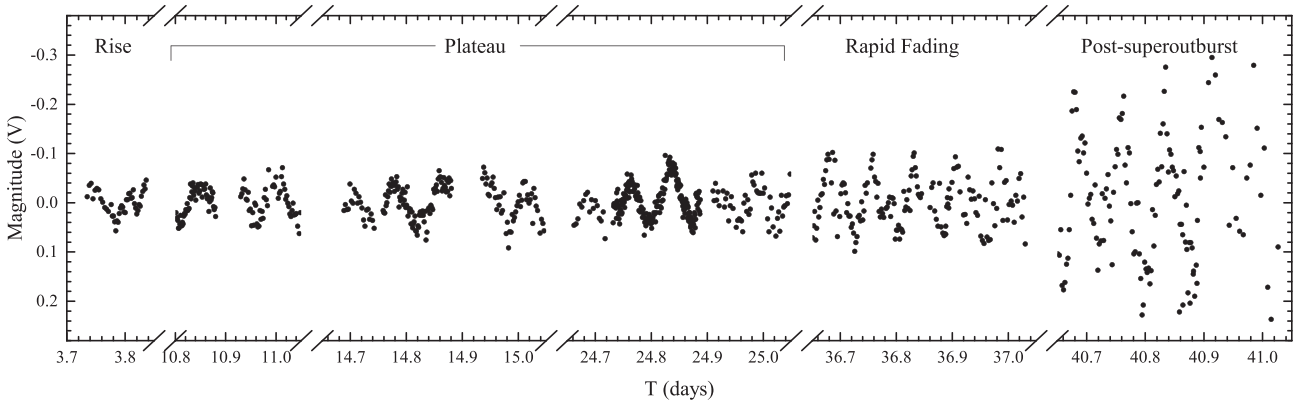

Figure 5. Six light-curve samples from different stages of the superoutburst of SSS J122222 (with the means and linear trends subtracted for each night).

superoutburst level in a week. On $T \simeq 52$–55, the days of the reddest optical spectrum, the UV flux dropped again, producing another red jump in the *uvm2-V* curve.

3.2 Development of superhumps

3.2.1 Superoutburst superhumps

Photometric modulations, known as superhumps, are clearly visible in the light curve of SSS J122222 from our very first time-resolved observations. Fig. 5 shows six light-curve samples which illustrate the development of superhumps during the superoutburst stage. It is known that the period of superhumps $P_{\rm sh}$ in SU UMa stars is not stable, but changes during a superoutburst in a complex way. An extensive study of SU UMa superhumps showed that the evolution of their periods is often composed of three distinct stages (see Kato et al. 2009, and their later papers). These complex period changes can be explained by variation of the accretion disc radius during a superoutburst (Hirose & Osaki 1990), which is possibly accompanied by variable gas pressure effects in the disc (Osaki & Kato 2013). The evolution of the superhump period in SSS J122222 has been investigated by Kato et al. (2013). Here we extend their analysis. In order to examine the evolution of superhumps, we determined the times of superhump minima and their amplitudes by fitting a sine wave to nightly light curves. The resultant O–C diagram and the superhump amplitudes are shown in the middle and top panels of Fig. 6, respectively.

Although the superhump period in SSS J122222 evolved rather differently to other SU UMa dwarf novae (see Kato et al. 2013 for a discussion of possible causes), nevertheless our analysis confirmed that the superhumps experienced three stages of their evolution as seen from the O–C diagram. The latter shows three distinct segments, which we identified and marked in Fig. 6 as stages A, B and post-superoutburst, following Kato et al. (2013). Fig. 7 shows the Lomb–Scargle periodograms calculated for different time intervals. The linear rise of the stage A segment of the O–C diagram (until $T \sim 20$) indicates an approximately constant period. The superhump amplitudes grew from ∼0.04 mag at the beginning of the stage to ∼0.07 mag at its end. Using the data for $T = 4$–14 and 15–21, we determined the periods of superhumps for these dates to be 111.26(4) and 110.64(6) min, respectively. The periods and their errors were computed using a linear fit to the corresponding segment of the O–C diagram. During the following ∼18 d ($21 \lesssim T \lesssim 38$) of stage B the superhumps also had a nearly stable, but shorter period of 110.10(2) min determined using the data for $T = 23$–34.

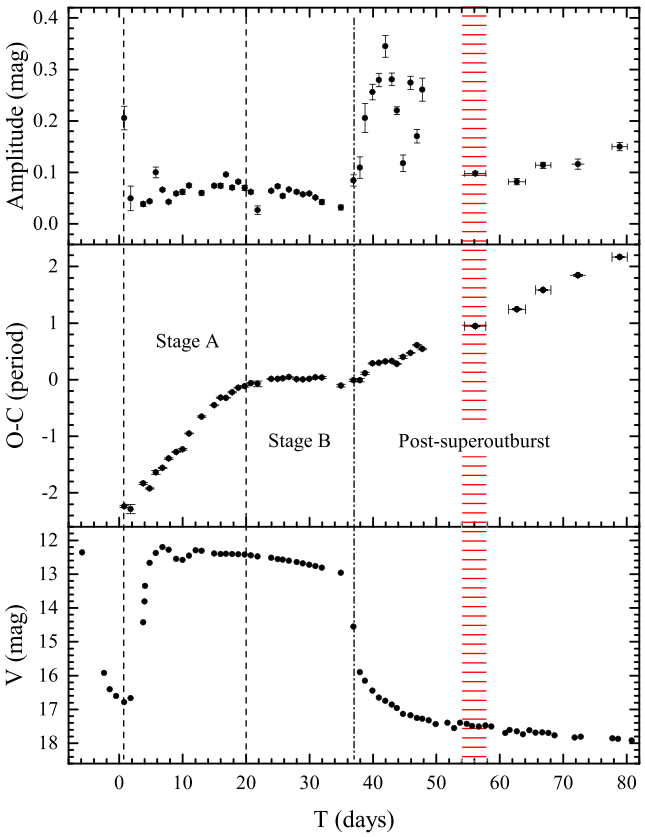

Figure 6. Top: the amplitudes of superhumps in SSS J122222. Middle: the O–C diagram of superhumps. A period of 110.09 min was used for the calculations. Bottom: the *V* light curve. The red vertical ribbon marks the days of the reddest optical spectra. The stages of the superhump evolution are marked following Kato et al. (2013).

To the end of this stage the amplitudes decreased to ∼0.04 mag, but started growing again after the transient had faded. The third segment of the O–C diagram ($T \gtrsim 38$) has an uneven, stepped structure, indicating sudden changes of the period. The duration of segments with a stable period is about 4 d. The superhump amplitude reached ∼0.3 mag, but showed short-duration decreases at the time of the period changes. Using the data for $T = 39$–51, we determined the mean period of superhumps to be 110.40(7) min. The periods of superhumps we find are consistent with those reported by Kato et al. (2013). The variation of superhump profiles during

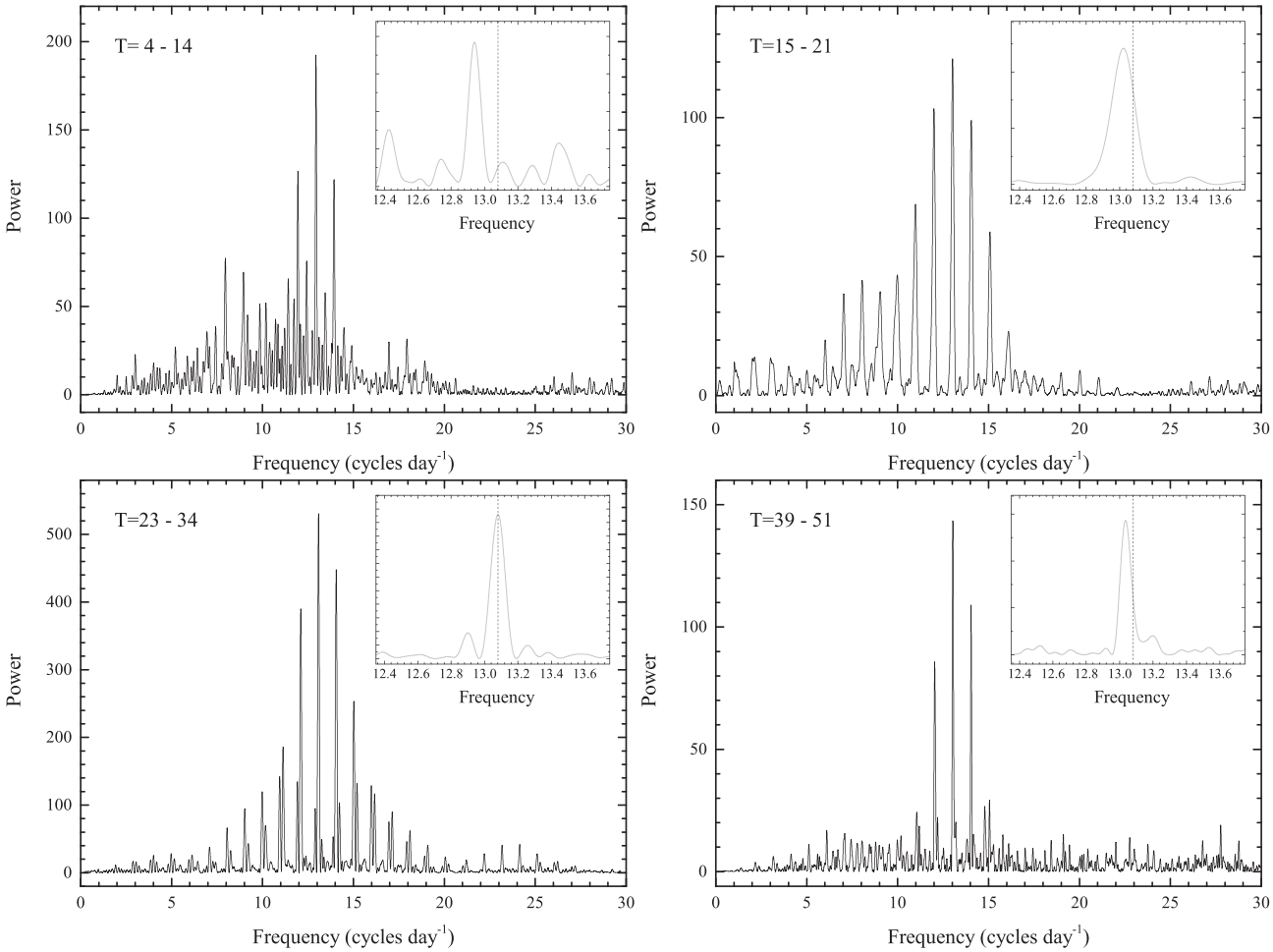

Figure 7. Lomb–Scargle periodograms of the V data combined among $T = 4$–14, 15–21, 23–34 and 39–51. The inset shows the enlarged region around the frequency 13.08 cycle d^{-1} – the averaged frequency of superhumps during the superoutburst stage B, marked by the vertical dashed line.

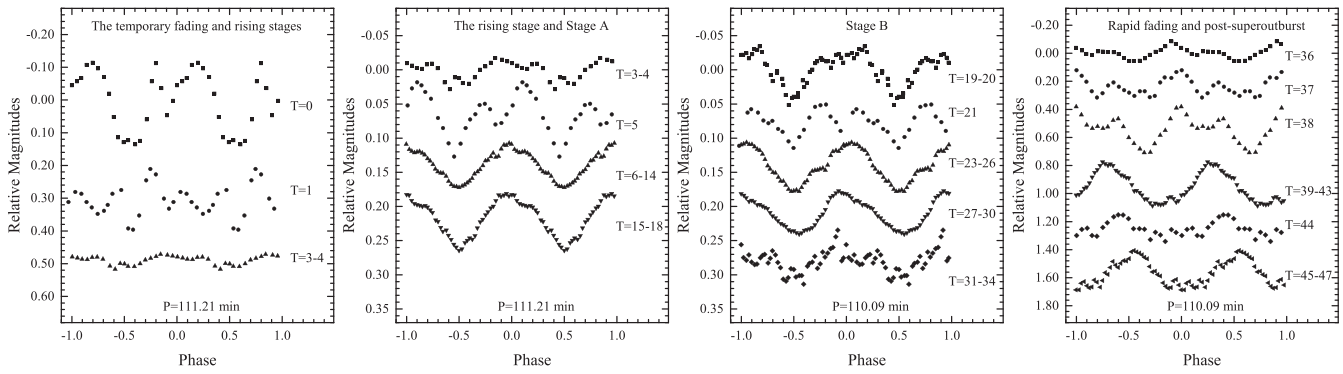

Figure 8. Variation of superhump profiles during the superoutburst of SSS J122222.

the superoutburst is shown in Fig. 8. Most of the time the modulations had a nearly symmetric, sinusoidal profile, although there were several occasions when the superhump profiles transformed from single-humped to double-humped and back.

Our multicolour photometry shows that the superhumps were redder at their light maximum (Fig. 9). Such a behaviour is in general agreement with previous reports (Schoembs & Vogt 1980; Hassall 1985; Isogai et al. 2015). This can be explained by assuming that the superhump light source (SLS) is an expanded low-temperature area in outer regions of the accretion disc (see e.g. Warner 1995; Uemura et al. 2012, and references therein). We note, however, that not only the period, amplitude and profiles of superhumps had changed over the course of the superoutburst. Fig. 9 displays a notable difference in the colour profiles of superhumps at different stages of superhump evolution. During the stage A the superhump colour variability was rather weak, but it significantly increased after the transition to the outburst stage B. This indicates that the accretion disc at the superoutburst plateau stage experiences more complex evolution than just the variation of its radius, suggesting substantial expanding of the SLS area or/and lowering of its temperature.

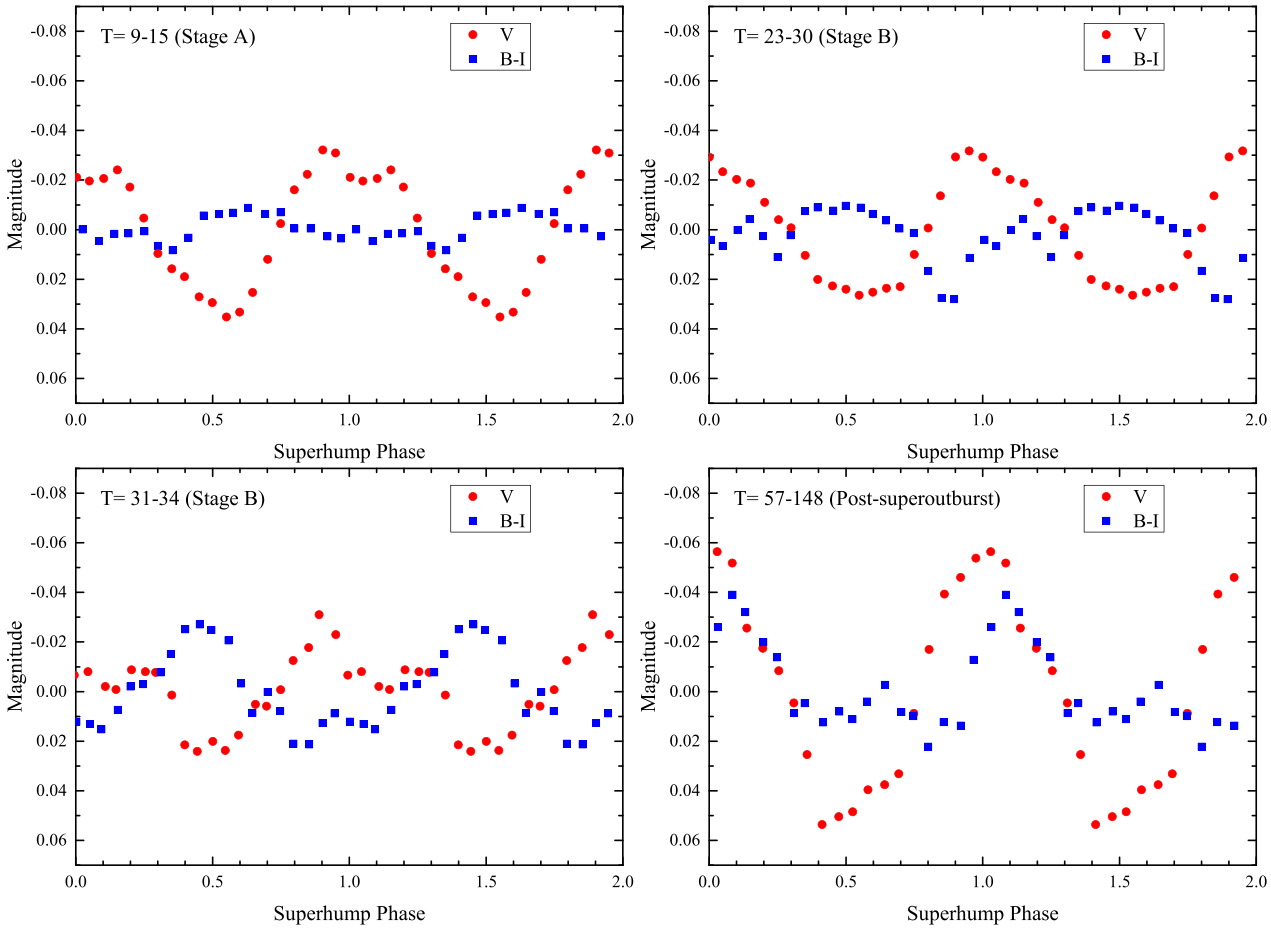

Figure 9. Phase-averaged *V* light curves and *B–I* colour variations of superhumps at different stages of the superoutburst of SSS J122222.

3.2.2 *Post-superoutburst modulations*

A visual inspection of the data revealed the presence of persistent modulations in the light curve long after the superoutburst. We show below that a period of these modulations is longer than that of the stage B superhumps, thus also implying their superhump nature. We traced them until the end of our time series observations in 2015. In order to explore these modulations, we first studied the observations obtained in 2013 after the rapid fading phase. We divided this light curve into short pieces of a 3–6 d duration and analysed them separately. We found that since at least $T = 53$ the modulation had a very stable period. The Lomb–Scargle periodogram of the *V* data combined between $T = 53$ and 148 shows a very narrow and strong peak at 13.0261 cycle d^{-1} (Fig. 10, left-hand panel). Folding short subsets at the period 110.547 min results in modulations of similar amplitude which are all in phase with each other (Fig. 10, right-hand panel). The shape of the average profile very much resembles a typical superhump profile (see e.g. fig. 1 in Kato et al. 2009). The colour variability of these post-superoutburst superhumps had changed significantly when comparing with the superhumps observed during the outburst stage (Fig. 9). The period of these post-superoutburst superhumps is about 0.4 per cent longer than that of the stage B superhumps.

The modulations were still strong in 2014 ($T = 399$–455), although during this season they were superposed on a longer-term variability with a time-scale of 8–12 h, which resembles so-called 'brightenings' observed in a few other WZ Sge-type systems, i.e. in V406 Vir (Zharikov et al. 2006; Aviles et al. 2010). This longer-term variability produces in the power spectrum an excess of power at low frequencies of 2–3 cycle d^{-1} (Fig. 11, left-hand panel, the red spectrum), making it difficult to study the superhump modulations. For this reason, we first detrended each night's light curve by a second-order polynomial. The Lomb–Scargle periodogram of this detrended data set is dominated by two sharp peaks with frequencies of 12.78 cycle d^{-1} (112.6 min) and its first harmonic, and of 18.72 cycle d^{-1} (76.9 min, Fig. 11, left-hand panel, the blue spectrum). The period of the 112.6 min modulation is ∼1.8 per cent longer than the period of the post-superoutburst superhumps observed in 2013. The modulations seemed very stable. Folding short subsets of the 2014 light curve at the 112.6 min period results in profiles of similar amplitude which are all in phase with each other (Fig. 11, right-hand panel). The origin of the 18.72 cycle d^{-1} peak in the power spectrum is unclear.

The most recent time-resolved observations, obtained in 2015 ($T = 740$–763), basically confirmed the photometric behaviour observed in 2014. However, the time series analysis may suggest that superhumps were finally replaced by orbital variability. There is a peak in the power spectrum (see the inset in Fig. 11, left-hand panel) coinciding with the orbital frequency of 13.112 cycle d^{-1}, derived from spectroscopic data in Section 4.2. Unfortunately, most of the 2015 data are quite noisy and of a short duration. The aliasing problem prevents us from claiming a detection of the orbital signal in the optical light curve.

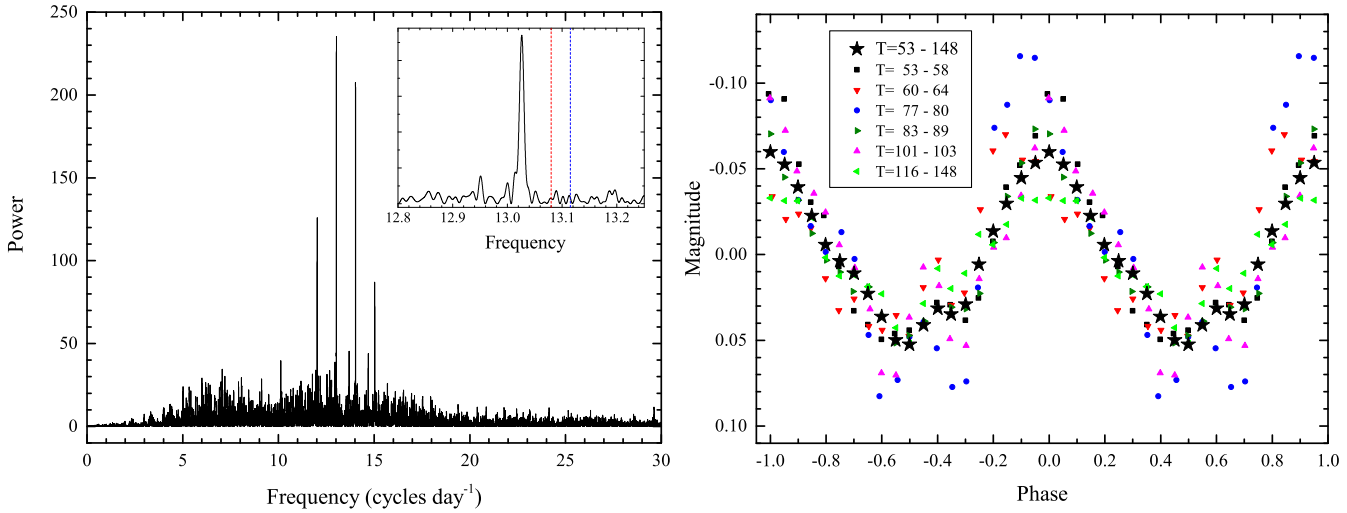

Figure 10. Left: Lomb–Scargle periodogram of the V data combined between $T = 53$ and 148. The inset shows the enlarged region around the frequency 13.026 cycle d^{-1} – the frequency of post-superoutburst modulations observed in 2013. The vertical dashed lines mark the orbital (blue) and stage B superhump (red) frequencies of 13.11 and 13.08 cycle d^{-1}, respectively. Right: the entire set (large stars) and short subsets (small symbols) of the V data between $T = 53$ and 148, folded according to ephemeris $HJD_{\max} = 245\,6300.0610(3) + 0.076\,768\,87(5)E$.

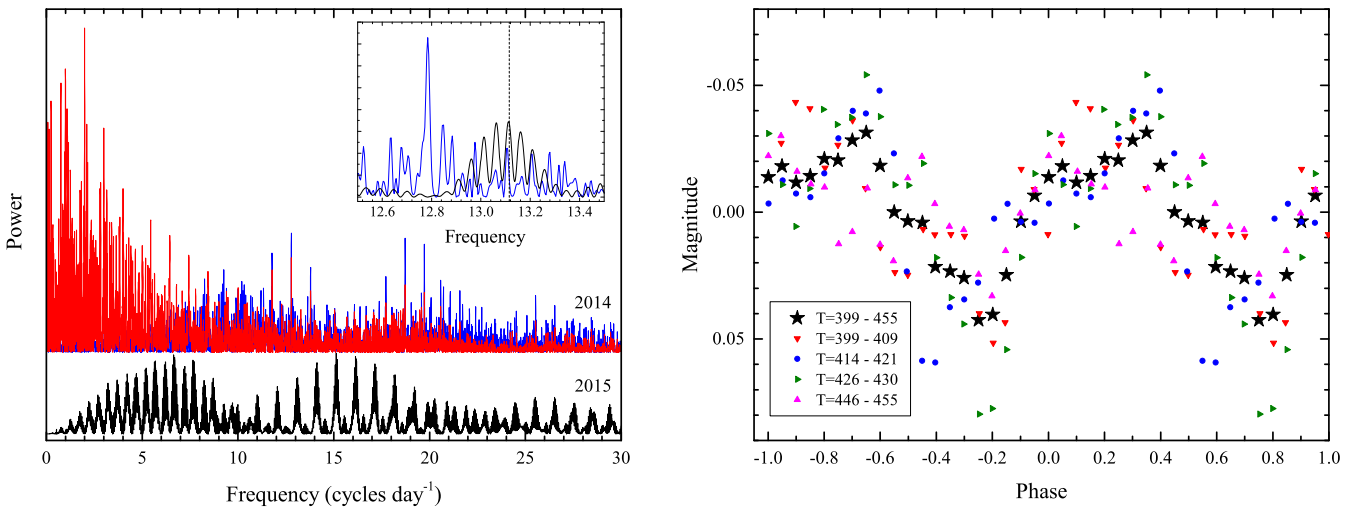

Figure 11. Left: Lomb–Scargle power spectra for optical data of SSS J122222 obtained in 2014 ($T = 399$–455, two upper spectra) and 2015 ($T = 740$–763, a bottom spectrum). The red line represents the spectrum for the original 2014 photometry, whereas the blue and black lines are for the detrended data. The inset shows the enlarged region around the orbital frequency marked by the vertical dashed line. Right: the entire set (large stars) and short subsets (small symbols) of the detrended data, obtained in 2014 and folded with the period of 112.6 min.

Thus, our observations showed that long after the superoutburst SSS J122222 was still exhibiting very stable superhumps, with a period longer than that of the stage B superhumps. Post-superoutburst superhumps, also called 'late superhumps' (Vogt 1983), were observed in several other WZ Sge-type objects (see Kato, Maehara & Monard 2008; Kato 2015, and references therein). In SSS J122222, however, they were detectable for significantly longer time than in any other system. In Section 6.2 we discuss these late superhumps in more detail.

3.3 An ∼180-min variability

The periodograms of most segments of the light curve of SSS J122222 show an excess of power around frequencies ∼6–9 cycle d^{-1} with the strongest peak at ∼8.0 cycle d^{-1} (180 min, Figs 7 and 10). This signal was most evident during the outburst stage A. It then weakened, but was still detectable long after the superoutburst. We note that the global power spectrum in this frequency range is complex, suggesting a lower degree of coherence, though between $T = 4$ and 21 the signal was rather stable. Fig. 12 shows the V light curves from the time intervals $T = 4$–14 and 15–21 folded with the period of 180.48 min and averaged in 20 phase bins.

A period of 180 min is not directly related to superhump or orbital periods of SSS J122222 ($P_{\rm orb} = 109.80$ min; see Section 4.2), which are significantly shorter. We note that there are known a few other short-period CVs which exhibit variabilities with a period of a few hours, longer than the orbital one (e.g. GW Lib – Vican et al. 2011; FS Aur – Neustroev 2002; V455 And – Araujo-Betancor et al. 2005). Among those systems only in FS Aur is such a period very coherent over many years (Neustroev et al. 2013). It was proposed that the precession of a fast-rotating magnetically accreting WD can successfully explain this phenomenon (Tovmassian et al. 2003;

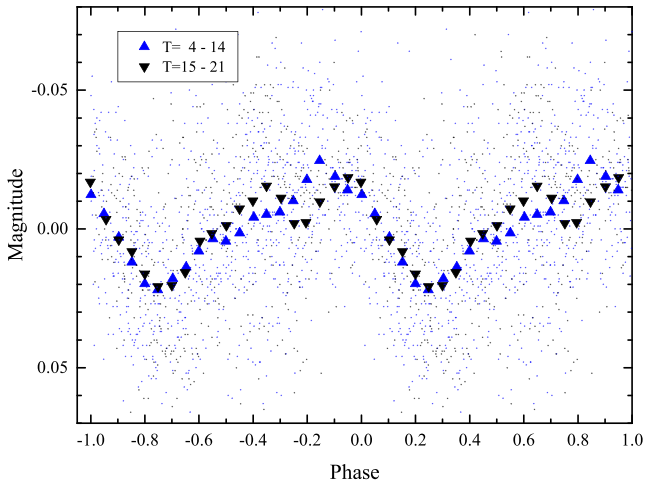

Figure 12. The V light curves from the time intervals $T = 4$–14 and 15–21 folded with the period of 180.48 min and averaged in 20 phase bins. The small and large symbols represent the individual observations and the data averaged in 20 phase bins, respectively. All data are plotted twice for continuity.

Tovmassian, Zharikov & Neustroev 2007). However, in other objects long-period modulations show a significantly lower degree of coherence (Araujo-Betancor et al. 2005; Vican et al. 2011), similarly to SSS J122222. There is currently no physical explanation for the latter phenomena.

4 OPTICAL SPECTROSCOPY

4.1 Spectral evolution throughout the superoutburst

Fig. 13 displays the spectral evolution of SSS J122222 through all the outburst stages and the following decay (the epochs of optical spectra are shown in Fig. 1). Note that during the superoutburst plateau the spectra changed very little, hence we show only the averaged outburst spectrum ($T = 20$–34).

At the temporary fading stage ($T = -1$ and -2), the spectra exhibit strong, very broad and double-peaked Balmer emission lines and weak emission lines of neutral helium (4471, 5876, 6678 Å). There is also a hint of a broad feature around 4700 Å that can be associated with the Bowen blend, He II λ4686 and He I λ4713.

During the plateau stage ($T = 20$–34) most of the emission lines were replaced by the broad absorption troughs with weak emission cores. Among the Balmer series lines, only Hα was still in emission, even though the broad absorption wings also showed up around the line. The full width at zero intensity (FWZI) of the absorption troughs corresponds to a velocity of ∼6800 km s^{-1}, which is very close to the fairly extreme width of the emission lines (FWZI ∼ 7000 km s^{-1}) observed during the temporary fading. It can be explained by the broadening effect of rapid rotation of the innermost parts of the optically thick accretion disc. An interesting feature is that those absorption components are clearly redshifted relative to the emission core, which are seemingly always centred close to the rest wavelength (Fig. 14, left-hand panel). By fitting a Gaussian to the absorption component of Hβ and Hγ in nightly averaged outburst spectra, we found a consistent and steady offset of ∼180–200 km s^{-1} from the rest wavelength. At the superoutburst plateau the C III/N III–He II complex and He I λ5876 and λ6678 lines were still in emission. Also, an emission bump centred at ∼5830 Å appeared. This bump is probably a blend of C III λ5827 and the C IV lines at λ5801 and 5812 Å, and possibly of other highly excited species on the shortward side of He I λ5876. In addition, the spectra show the appearance of the sodium D doublet (Na D λ5890/5896) in absorption. These lines are very uncommon for CV spectra. Although the sodium doublet is one of the strongest interstellar lines, it is not expected to be seen in the spectra of CVs because of their relatively close proximity. Nonetheless, Na D in absorption was noticed in spectra of several WZ Sge-type systems at different stages of their superoutbursts (Patterson et al. 1998; Nogami & Iijima 2004; Nogami et al. 2009), but it was not seen in other dwarf novae showing large amplitude outbursts (e.g. BZ UMa; Neustroev, Zharikov & Michel 2006).

After the rapid fading the emission bump at ∼5830 Å disappeared, but all the absorption lines transitioned from absorption to emission. Na D also appeared in emission, distorting the red wing of the double-peaked He I λ5876 line in all post-outburst spectra, even three years after the superoutburst (see Fig. 14, right-hand panel). We point out that Na D was also observed in emission in GW Lib some 40 d after the rapid fading phase (van Spaandonk et al. 2010). We also note the presence of a narrow, unidentified line at ∼5903 Å. This feature seems to be real and not noise or an artefact of the data reduction because it is present in different spectra and also exhibits a transition from absorption to emission, similarly to Na D.

As the system flux continued to decline, the emission lines got progressively stronger. In the spectrum taken during the decay phase on $T = 72$, the Hα has a moderate strength (EW = 129Å) and the Balmer decrement is relatively flat: Hα:Hβ:Hγ= 2.01:1.00:0.56. However, the final spectra taken in quiescence on $T = 848$ and 1127 show the extremely strong Hα line which peaks at eight and 11 times the continuum and has EW = 277 and 384 Å, respectively. To the best of our knowledge, this is the strongest emission line ever observed in a CV. The Balmer decrement is also very steep in these spectra: Hα:Hβ:Hγ= 3.20:1.00:0.44 ($T = 848$) and 3.42:1.00:0.56 ($T = 1127$). This change in the Balmer decrement from shallow to very steep indicates a transition from optically thick to optically thin conditions in the accretion disc. We also note that the spectra obtained on $T = 72$ and later show very wide symmetric absorptions at the wings of the Balmer lines (FWZI of the Hβ absorption is ∼19500 km s^{-1}). These absorption features are too broad to be produced in the Keplerian accretion disc and can only be formed in the high-density photosphere of the WD, indicating a very low accretion luminosity and mass-accretion rate. Under such conditions one could expect to see the donor star lines in red part of the spectrum; however there is no evidence at all for atomic lines (e.g. Na I λ8200) or molecular bands from the donor. We also note that the spectra from all available time-resolved data sets show no obvious radial velocity variability in the accretion disc emission lines. In Table 3 we present the equivalent width (EW) measurements of the most prominent lines measured from the averaged spectra.

4.2 Orbital period determination

The most direct method of estimating the orbital period of the binary system involves optical spectroscopy. We used the spectra taken during the superoutburst stage ($T = 28$–30) to identify the orbital period of SSS J122222. The chief problem was to identify the correct night-to-night alias and only these spectra had long enough duration while being taken over consecutive nights for this to be possible. At this stage the lines were in absorption and asymmetric, but in finding a period, one only requires detection of a periodic variation and any offsets are immaterial. We measured the radial velocity

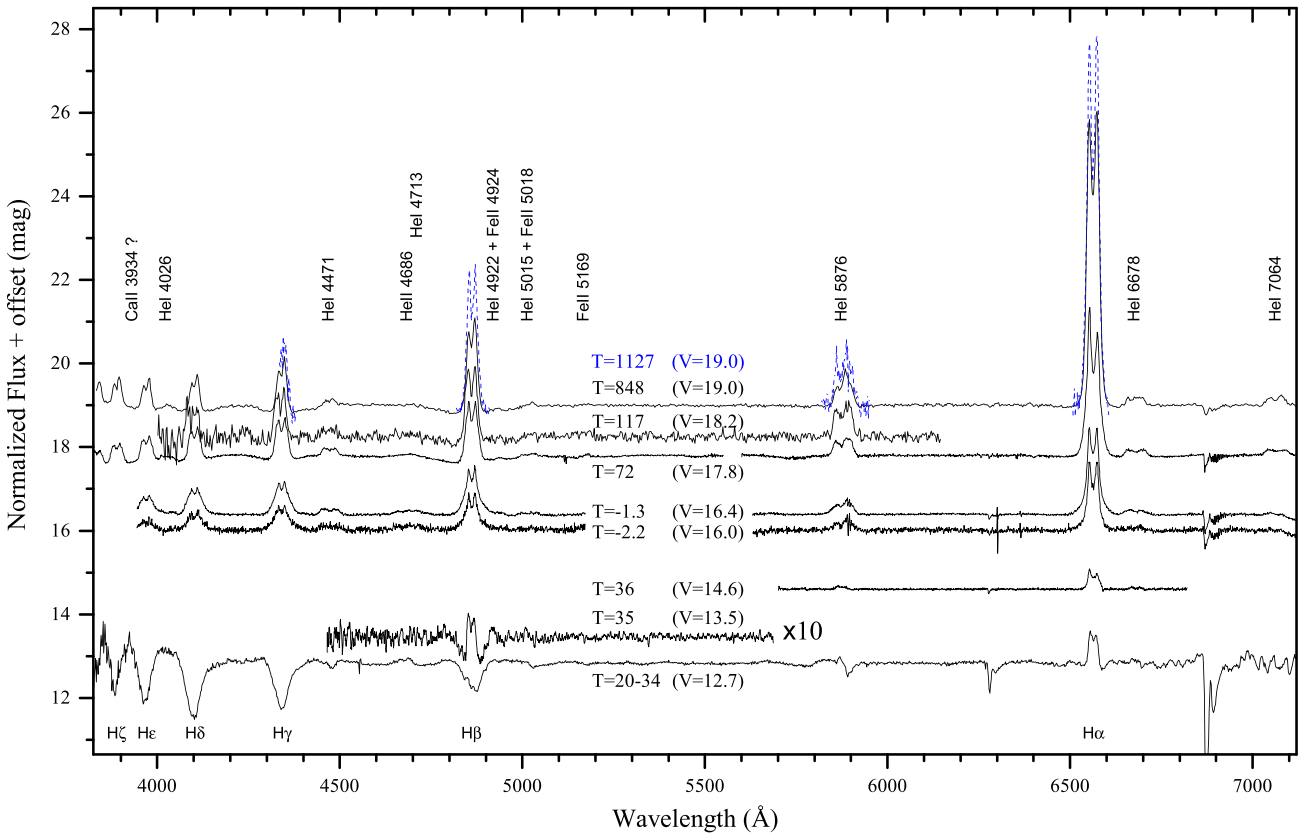

Figure 13. Spectral evolution of SSS J122222 through all the outburst stages and the following decay. All the spectra are normalized to the continuum flux and shifted with respect to each other in accordance to the magnitude of the system during the given spectral observation. Thus, the outburst spectra ($V \approx 12.7$) are at the bottom and the quiescent spectra ($V \approx 18$–19) are at the top of the figure. The $T = 1127$ spectrum is relatively noisy at the continuum level, therefore we only show the emission lines (a dashed blue line). Two lower outburst spectra are scaled up by a factor of 10 in relative intensity to magnify the spectral features and allow for a better comparison.

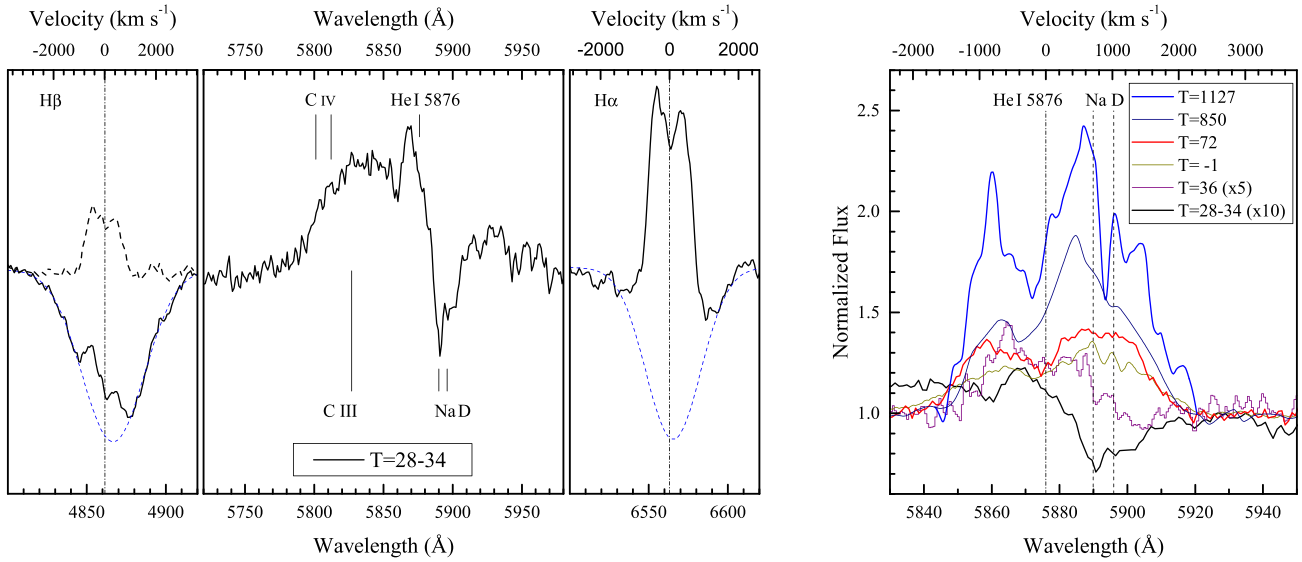

Figure 14. Left: Hα and Hβ line profiles and the region around the C III/C IV/He I λ5876/Na D complex (black solid line) during the plateau stage of the superoutburst (arbitrary scaling). The dashed blue line shows a Gaussian fit to the absorption components of Hα and Hβ. The dashed black line shows the profile of Hβ after being corrected for absorption. Right: He I λ5876 and Na D line profiles from different data sets, shown in actual scale (for a better comparison, the $T = 28$–34 and 36 profiles have been multiplied by a factor of 10 and 5, respectively).

Table 3. EWs of the most prominent lines measured from the averaged spectra. Negative values are used for *absorption* lines.

Epoch T	Hα	Hβ	Hγ	Hδ	He I λ5876 + Na D	He I λ4471	Magnitude (V)
–2	58.0 ± 0.9	32.5 ± 0.9	27.2 ± 0.6	18.4 ± 0.4	11.4 ± 0.9	5.6 ± 0.6	16.0
–1	81.8 ± 0.3	47.4 ± 0.4	34.6 ± 0.2	27.7 ± 0.2	16.5 ± 0.3	7.3 ± 0.3	16.4
28 – 34	2.0 ± 0.1	− 3.4 ± 0.1	− 5.3 ± 0.1	− 6.0 ± 0.1	0.3 ± 0.1	− 0.3 ± 0.1	12.7
35	...	− 2.1 ± 0.2	...	...	...	...	13.5
36	12.3 ± 0.2	...	...	...	1.7 ± 0.4	...	14.6
72	126.0 ± 0.3	62.6 ± 0.3	35.3 ± 0.3	26.2 ± 1.3	22.8 ± 0.9	8.2 ± 0.3	17.8
117	...	83.9 ± 1.6	40.7 ± 2.4	25.7 ± 4.2	38.7 ± 1.9	9.7 ± 1.4	18.2
850	277.3 ± 0.9	86.5 ± 0.2	38.5 ± 0.4	23.9 ± 0.4	31.6 ± 0.7	5.2 ± 1.0	19.0
1127	384.1 ± 8.5	112.2 ± 3.3	63.0 ± 5.0	...	51.3 ± 3.0	9.9 ± 2.3	19.0

Note. The Magnitude column indicates the approximate magnitude of SSS J122222 during the observation. They are taken from simultaneous or interpolated from recent photometric observations.

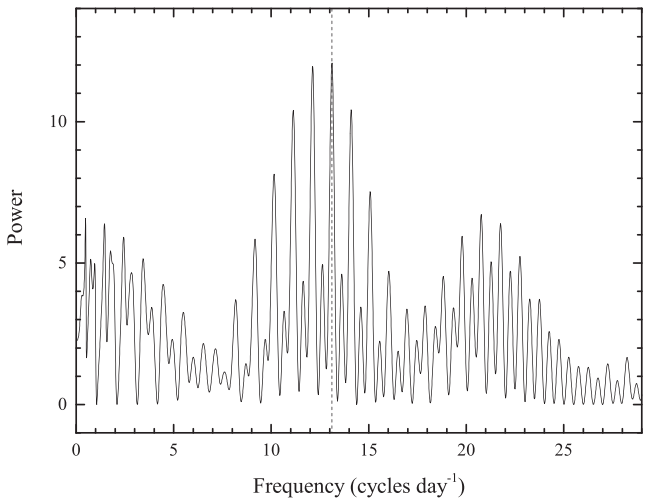

Figure 15. Lomb–Scargle periodogram for spectral data of SSS J122222 obtained during the $T = 28$–30 time interval. The vertical dashed line marks the orbital frequency of 13.112 cycle d^{-1}.

of Hβ, the profile of which showed the strongest variations, using cross-correlation with a single Gaussian (Schneider & Young 1980). This has one free parameter, the width of the Gaussian. We tried widths (FWHM) varying from 1500 to 3000 km s^{-1}. For each set of radial velocities, we computed 2000 Lomb–Scargle periodograms using bootstrap resampling, in each case retaining the period of the highest peak to build up statistics upon the reliability of the period identification. An example of the periodogram calculated for the FWHM of 2500 km s^{-1} is shown in Fig. 15. The results clustered around two peaks split by one cycle d^{-1} at frequencies of 12.127 and 13.112 cycle d^{-1}. Although the radial velocities alone do not quite secure the alias, we are sure that in fact the higher frequency peak of the pair corresponds to the orbital modulation. Indeed, the period of this modulation is only slightly longer than the period of the superhump signal, as expected for the traditional, 'positive' superhumps which are standard for this class of star. Otherwise, it will lead to the 'negative' superhumps with an unrealistically large difference between orbital and superhump periods.[5] Naturally, a more complete radial velocity data set is desirable to confirm this reasoning.

We thus determined the orbital period $P_{\rm orb}$ to be 109.80(7) min. This period is in the vicinity of a possible orbital period of 109.266 min identified by Kato et al. (2013). However, we could not confirm this value from our own analysis of both the CRTS data and our observations, whereas our late photometric data show a peak in the power spectrum coinciding with the adopted orbital frequency of 13.112 cycle d^{-1} (Fig. 11, left-hand panel).

4.3 Radial velocity study

Although our spectra do not show appreciable radial velocity variability, we made an attempt to measure or put the upper limits on the radial velocity semi-amplitudes of emission lines using the double-Gaussian method (Schneider & Young 1980). In order to test for consistency in the derived velocities and the zero phase, we separately used the emission lines Hα and Hβ from the $T = 72$ data set. Additionally, to improve the confidence and reliability of the obtained results, we also created the phase-binned spectra by averaging the individual spectra in 12 phase bins.

All the measurements were made using various Gaussian FWHMs of 50–300 kms^{-1} and different values of the Gaussian separation Δ ranging from 1000 km s^{-1} to 5000 km s^{-1} in steps of 100 km s^{-1}, following the technique of 'diagnostic diagrams' (Shafter, Szkody & Thorstensen 1986). For each value of Δ we made a non-linear least-squares fit of the derived velocities to sinusoids of the form

$$V(\varphi, \Delta) = \gamma(\Delta) - K_1(\Delta) \sin [2\pi\,(\varphi - \varphi_0\,(\Delta))] \qquad (1)$$

where γ is the systemic velocity, K_1 is the semi-amplitude, φ_0 is the phase of inferior conjunction of the secondary star and φ is the orbital phase calculated relative to epoch $T_0 =$ HJD 245 6372.65160.

The resulting diagnostic diagrams are shown in Fig. 16. We found the maximum useful separation to be $\Delta_{\rm max} \simeq 2800 - 3000$ km s^{-1} for both lines until the noise in the line wings begins to dominate. K_1, γ and φ_0 are quite stable over a reasonable range of Gaussian separations around $\Delta_{\rm max}$, thereby helping us with their choice. Both the tested lines show very consistent results, and we adopted the following values of the orbital parameters: $K_1 = 16 \pm 5$ km s^{-1},

[5] 'Negative' superhumps, which are modulations with a period a few per cent shorter than the binary's orbital period, are sometimes observed in CVs (see e.g. an analysis of the *Kepler* data of V344 Lyr by Wood et al. 2011). In most cases they appear in quiescence and sometimes can survive a normal outburst (Wood et al. 2011; Osaki & Kato 2013). However, in rare cases when the negative superhumps were detected in superoutbursts, they were significantly weaker than normal, positive superhumps (Osaki & Kato 2013). Thus, we have no doubt that all the observed superhumps in SSS J122222 were of the normal, positive type.

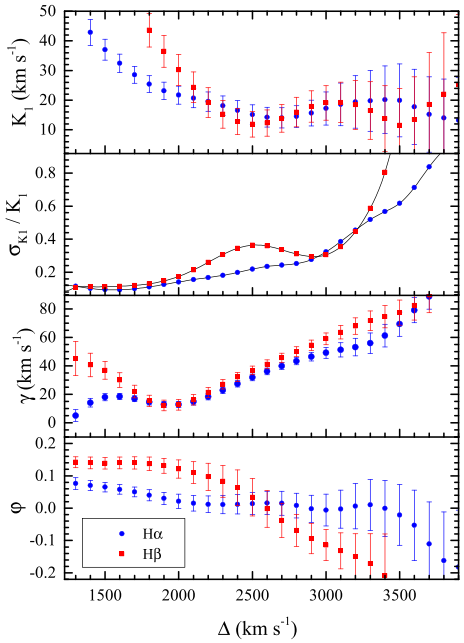

Figure 16. The diagnostic diagram for the Hα and Hβ emission lines from the $T = 72$ observations, showing the response of the fitted orbital elements to the choice of the double-Gaussian separation.

$\gamma = 44 \pm 6$ km s^{-1} and $\varphi_0 = 0.00 \pm 0.06$. The formal errors are the standard deviations of the least-squares fits. They most likely underestimate the true errors, as they may not include a priori unknown systematic effects. Moreover, it is well known that the parameters obtained with the double-Gaussian method are often affected by systematic errors. Thus, the derived value of K_1 should be used with great caution.

5 THE SPECTRAL ENERGY DISTRIBUTION

5.1 The SED evolution

Using our multicolour observations, we have reconstructed the spectral energy distribution (SED) of SSS J122222 in the UV–optical–NIR wavelengths at several key moments of the superoutburst, the following decay and quiescence (Fig. 17). We note that although the SED in quiescence was created from the most recent observations obtained in 2016 April (T = 1186–1196), its UV–optical segment coincides precisely with the two previous multiband observations (T = 536 and 737). In addition, we show the archival pre-outburst observations taken by the Wide-field Infrared Survey Explorer (*WISE*) observatory in the IR band on $T = -920$. We also examined NEOWISE-R[6] Single Exposure Source Table and found at least six sources which are a very good positional match to SSS J122222. All these observations were made between $T = 368$ and 906, i.e. when SSS J122222 was already close to or in quiescence. Although the signal-to-noise ratio of this photometry is low (∼3), all the measurements in the W1 filter (3.4 μm) are consistent with the pre-outburst *WISE* observations, giving the same average magnitude of 16.55. This allowed us to include the pre-outburst W1 and W2 (4.6 μm) measurements in the current SED in quiescence.

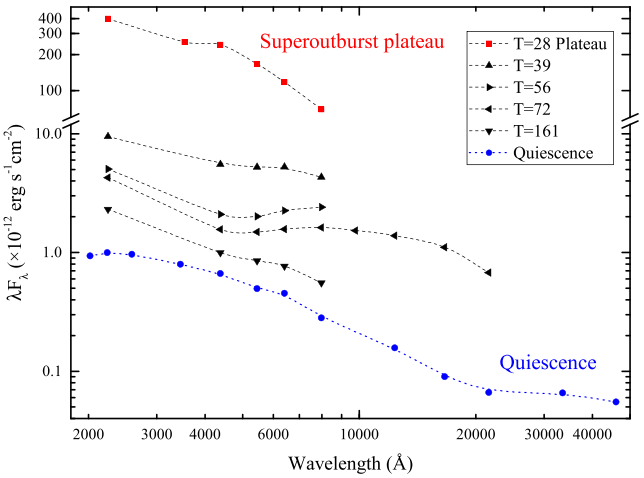

Figure 17. The SED of SSS J122222 at several key moments of the superoutburst, the following decay and quiescence. The SED in quiescence is created from the most recent observations taken in 2016 April (T = 1186–1196).

The SED shows a complex transformation through the superoutburst and the following decay. Its UV–optical part during and after the active stage was evolving in a similar manner to previous observations of outbursts (see e.g. Verbunt 1987; Warner 1995), indicating the evolution of the accretion disc and boundary layer, and the possible cooling of the accretion-heated WD. On $T = 28$, the flux from the V to I bands had a slope $\alpha = 3.29 \pm 0.07$ ($f_\lambda \propto \lambda^{-\alpha}$) that is close, but still less than the Rayleigh–Jeans tail of an accretion disc spectrum. After the rapid fading phase, a strong red-NIR excess emerged, peaking at 8000–10 000 Å, which disappeared about 100 d later. In quiescence, the flux in the red-NIR part of the spectrum (from R to Ks bands) is linearly decreasing (in log–log space), having a slope $\alpha = 2.66 \pm 0.06$, and the SED shows no sign of any excess in the red-NIR wavelength range.[7] We note that the appearance and disappearance of the excess cannot be connected with the donor star, for example with one of its side heated during the outburst, because strong orbital variability of the light and its colours is expected in this case, which we were unable to detect in our multicolour data. To the best of our knowledge, such a phenomenon has never been reported before. We discuss it in Section 6.3.

5.2 The SED in quiescence

Well into quiescence the spectra of SSS J122222 show no sign of the donor star. However, at orbital periods of ∼2 h normal CVs have relatively bright donor stars. Although in most CVs there is still a substantial contamination of the NIR luminosity by the accretion process, which makes the detection of their donor stars difficult (Hoard et al. 2002), sometimes the donor can directly be recognized by observing the red-NIR hump in the SED (Harrison et al. 2013), or after subtracting the disc contribution in the NIR

[6] The *WISE* was placed into hibernation in 2011 February. The survey continued as NEOWISE (Mainzer et al. 2011), when the spacecraft was brought out of hibernation. NEOWISE observations in the 3.4 and 4.6 μm bands were resumed in 2013 December.

[7] The *WISE* data may indicate the presence of an additional source of emission at mid-IR wavelengths (3.4–4.6 μm), resembling the SEDs of several other CVs, including the prototype system WZ Sge. This mid-IR excess is usually attributed to dust (see Howell et al. 2008 and therein), although Harrison et al. (2013) questioned this interpretation.

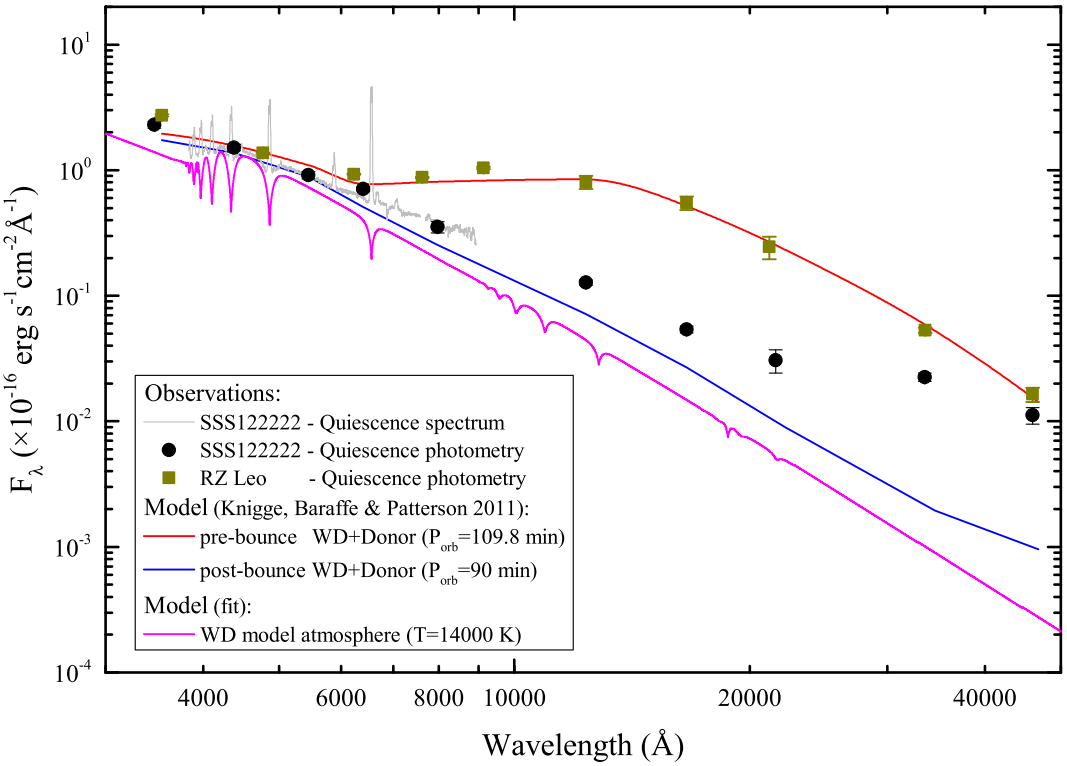

Figure 18. Theoretical SEDs of pre- and post-bounce CVs, based on the models of Knigge et al. (2011), shown together with the photometric and spectroscopic data of SSS J122222 and RZ Leo in quiescence (see text for details).

from the observed data (Ciardi et al. 1998). In CVs in which a contamination of the NIR luminosity by the accretion disc is less significant due to a low mass-transfer rate, the NIR hump should be more pronounced (see e.g. the SED of the WZ Sge-type dwarf nova RZ Leo in Mennickent et al. 1999, and also Fig. 18 and the discussion below) and the donor star can also be visible through its absorption lines (see e.g. Ishioka, Sekiguchi & Maehara 2007; Hamilton et al. 2011; Harrison 2016). On the other hand, the donor in a period bouncer should be so dim that even the accretion-heated WD alone is expected to outshine the donor at optical and the NIR (Knigge 2006).

SSS J122222 is one such system, in which the contribution of the accretion disc to the continuum is very low, as evident from extremely strong emission lines and clearly seen absorption lines of the WD. On the other hand, its orbital period is relatively long, meaning that a near-main-sequence donor star should be relatively bright. According to the semi-empirical donor star sequence presented by Knigge et al. (2011), a normal donor in SSS J122222 should have the absolute magnitudes $J \approx 9.3$, $H \approx 8.7$ and $Ks \approx 8.4$. In order to compare these with the apparent magnitudes, one needs to scale the former to the distance of SSS J122222. The distance to a SU UMa CV can be estimated by utilizing the empirical relationships between absolute magnitude and orbital period of dwarf novae at the superoutburst plateau and at maximum light derived by Patterson (2011). For SSS J122222, these relationships give ∼275 pc for an average binary inclination i of 57°, which can be adopted as a reasonable value. Indeed, the broad double-peaked emission line profiles in spectra of SSS J122222 suggest a relatively high inclination. On the other hand, the extensive photometry and spectroscopy of SSS J122222 rule out any significant eclipse, which constrains the inclination i to be less than about 70° to avoid an obvious partial eclipse of the disc. Moreover, the inclination is expected to be even less because the peak-to-peak separation of the emission lines in SSS J122222 is significantly smaller than in highly inclined CVs (compare 940 km s^{-1} in SSS J122222 and, e.g. 1150 km s^{-1} in the eclipsing CV HT Cas of similar $P_{\rm orb} = 106$ min – Neustroev, Zharikov & Borisov 2016 – whose inclination is 81°). Therefore, we adopted the source distance to be 275 pc with a realistic error on the distance of about ± 75 pc (for a discussion on uncertainties, see Patterson 2011). However, bearing in mind the unusual properties of SSS J122222, we caution the reader that this distance estimate may be less accurate. Thus, the apparent *JHKs* magnitudes of a normal donor star in SSS J122222 should be ∼16.4, 15.8 and 15.5 ± 0.6 mag, respectively. This is about two magnitudes brighter than the observed magnitudes of SSS J122222 (Table 1), even *without* taking into account of any contribution from the accretion disc and WD, implying thus that the donor star in SSS J122222 is of very low luminosity.

We find it instructive to compare the observed SED of SSS J122222 in quiescence with the expected SEDs of a CV at different evolutionary stages. For this, we used the models of Knigge et al. (2011) which utilize a semi-empirical CV evolution track based on the observed mass–radius relationship of their donor stars. Tables (tables 5– 6 and 7– 8) from their work provide the predicted absolute magnitudes of the donor star and the WD along the CV evolution sequence for a CV before and after the binary has reached the period minimum. For the pre-bounce case, we combined the fluxes of the donor and WD in a CV with $P_{\rm orb} = 109.8$ min. For the post-bounce case we summed the component fluxes of a CV with $P_{\rm orb} = 90$ min, the longest calculated post-bounce period.[8] In these

[8] Note that the donor flux and accordingly its contribution to the total flux are expected to decrease towards longer post-bounce periods.

calculations, no contribution from an accretion disc was taken into account, thus the calculated SEDs should be considered as a lower limit to the actual SEDs. For a comparison, we also calculated a model atmosphere spectrum of a WD with a mass of 0.9 $M_\odot$ and a surface temperature of 14 000 K, which reproduces the observed broad wings of Balmer line profiles and the calculated flux of which is in good agreement with the adopted distance.[9]

All the calculated SEDs were then scaled to the distance of SSS J122222, 275 pc. They are shown in Fig. 18 together with the photometric and spectroscopic data of SSS J122222 in quiescence. For a comparison, we also show the photometric data of RZ Leo, another WZ Sge-type CV, which has a similar orbital period (109.5 min) and which shares many properties with SSS J122222 (Mennickent et al. 1999; Mennickent & Diaz 2002). In particular, the disc contribution to the spectrum of RZ Leo is also insignificant and probably even smaller than in SSS J122222, as indicated by deep WD absorption lines clearly visible in the SDSS spectrum. We point out that in contrast to SSS J122222, the donor star of M5 spectral type is easily seen in the spectrum of RZ Leo, confirming the pre-bounce status of the system (Mennickent & Diaz 2002; Hamilton et al. 2011). Thus, RZ Leo represents a good test case for comparing the observed and calculated SEDs. For this analysis, we used the available photometric measurements of RZ Leo from the SDSS, 2MASS and *WISE* data bases. Although the distance to RZ Leo is estimated to be 260 ± 60 pc (Patterson 2011), also very close to SSS J122222, we rescaled the fluxes to 275 pc.

The observed SEDs of SSS J122222 and RZ Leo show a close resemblance in the optical wavelengths, but a significant difference in the NIR. RZ Leo follows the predicted pre-bounce SED surprisingly well, whereas the observed NIR flux of SSS J122222 is much lower (7–10 times in the *JHKs* bands) than expected from a CV with a normal donor star; therefore, a main-sequence donor is excluded. However, the observed NIR flux is about two to three times higher than the sum of the predicted fluxes from the WD and a post-period-minimum donor. This excess can possibly be explained by a contribution from the accretion disc. Although the optical continuum flux from the disc in SSS J122222 is low, nonetheless it can be more significant at NIR wavelengths (Hoard et al. 2002).

6 DISCUSSION

The analysis of observations of SSS J122222 presented above shows a number of features, many of which are rare or quite unusual when compared with most of WZ Sge-type systems and even any other dwarf novae. Here we merely highlight and discuss a few most interesting points.

6.1 Mass ratio *q*

The light curve of SSS J122222 is remarkable for its double superoutburst with a deep and prolonged dip between its two segments, a long duration of the second superoutburst's segment, the longest of any other known dwarf novae, and its very gentle decline. Kimura et al. (2016) suggested that such double superoutbursts which were previously observed in only a few other WZ Sge-stars may indicate a very low q. Kato et al. (2014) presented a survey of the fading rates of about 320 superoutbursts of ∼185 ordinary SU UMa-type and 45 WZ Sge-type dwarf novae (for several objects more than one superoutburst were studied.). The fading rate during the superoutburst plateau in SSS J122222 was the slowest among all the studied superoutbursts. It was shown (Osaki 1989; Cannizzo et al. 2010) that the theoretical fading rate depends mostly on the accretion disc viscosity in the hot state, thus for slower fading rates one needs to consider a smaller viscosity. Kato et al. (2014) suggested that the viscosity should be smaller in CVs with a low mass ratio, therefore the unusually slow fading rates may also indicate a very low q (see section 5.5 in their paper for a more detailed discussion).

Kato et al. (2013) attempted to estimate q using the periods of superhumps during the rising stage and post-superoutburst stage and found that SSS J122222 has a mass ratio less than 0.05. Another approach to finding q is to employ the empirical relation between the fractional superhump period excess $\epsilon = (P_{\rm sh} - P_{\rm orb})/P_{\rm orb}$ and the mass ratio (Patterson et al. 2005). Because the period of superhumps is variable, it is not clear which value of $P_{\rm sh}$ should be used. In the literature, the mean superhump period or the period of stage B superhumps is often used. For SSS J122222 the latter period is 110.10 min and $\epsilon = 0.27(7)$ per cent. Vican et al. (2011) noted, however, that Patterson et al. (2005) calibrated their ϵ–q relation with superhumps observed during an early bright phase of the outburst. For SSS J122222 this corresponds to the second half of stage A ($P_{\rm sh} = 110.64$ min), which gives $\epsilon = 0.76(8)$ per cent. Thus, the period excess in SSS J122222 is one of the smallest known of all CVs showing superhumps. For $\epsilon = 0.27$ and 0.76 per cent the ϵ–q relation of Patterson et al. (2005) gives the mass ratio 0.015 and 0.045, respectively. In order to be on the conservative side and bearing in mind that the ϵ–q relation is poorly calibrated for low q, we adopt the larger value as an estimate of q. This is consistent with the value reported by Kato et al. (2013), and also in good agreement with the measured K_1. Indeed, by using the WD mass $M_{\rm wd} = 0.9\ M_\odot$ and the inclination $i = 57^\circ$, adopted in Section 5.2, the mass function gives $q = 0.04$.

6.2 Late superhumps

At least 111 d after the rapid fading phase SSS J122222 had been still exhibiting very stable modulations with a period longer than that of the stage B superhumps. This is in general agreement with the previous observations of other WZ Sge-type objects (see Patterson et al. 1998; Kato et al. 2008; Kato 2015, and references therein), although in SSS J122222 these late superhumps were seen for significantly longer time than in any other WZ Sge-type system. Moreover, the stable modulations still persisted even about 420 d after the superoutburst, but their period has further increased by about 2 per cent. Unfortunately, we missed this period transformation and it is unclear if these most recent modulations are evolved late superhumps or they are another kind of quiescent superhumps. Quiescent superhumps were observed in several dwarf novae (e.g. in V1159 Ori – Patterson et al. 1995). Thanks to the unprecedented precision and cadence of *Kepler* long-term light curves of V344 Lyr and V1504 Cyg, such modulations were traced throughout the decline phase of superoutbursts to quiescence and through a few following normal outbursts of these (ordinary) SU UMa-type stars (Still et al. 2010; Wood et al. 2011; Osaki & Kato 2013). However, they seem to not survive the whole superoutburst cycle as they were seen no later than about 40 d after superoutbursts ended (Osaki & Kato 2013), a much shorter time interval than in SSS J122222.

[9] Selected values of temperature and log g are not unique, slightly different solutions are plausible. Hence, the adopted parameters should be considered as a first approximation.

6.3 A massive cool gas region beyond the 3:1 resonance radius

Simultaneously with the start of the rapid fading phase, SSS J122222 showed the appearance of the strong red-NIR excess, which disappeared 100 days later. It is interesting to note that the passage through the reddest colours had been accompanied by alteration of the decline slope (Fig. 4), by a significant decrease of superhump amplitudes (Fig. 6), and perhaps by an emergence of the late superhumps (Section 3.2.2). This red-NIR excess and also the appearance of the Na D line in absorption during the plateau stage indicate a fairly cool region in the outer disc. Tovmassian & Zharikov (2013, and references therein) show that outer parts of extended accretion discs of period bouncers should indeed contain cool (∼2000 K) material unlike ordinary dwarf novae in which 5000 K is considered as the disc edge temperature. We suggest that this cool gas is accumulated in the outermost part of the disc, beyond the 3:1 resonance radius. In the binaries with low mass ratios such as the WZ Sge-type stars, the 3:1 resonance radius is located well inside the Roche lobe of the primary while the tidal truncation radius is almost as large as the Roche lobe. During energetic superoutbursts after the long period of quiescence, the disc expands in order to transfer the large amount of angular momentum released by the accreting matter. That can bring substantial mass beyond the 3:1 resonance radius. It is thought that during a superoutburst a significant fraction (70–80 per cent) of the disc is accreted (Cannizzo et al. 2012). However, the matter accumulated in the outer parts of the disc avoids the 3:1 resonance, suffers a lower tidal dissipation of angular momentum and may be left from being accreted during the main superoutburst (Hellier 2001).

Such a model was originally proposed to explain the repeated rebrightenings observed in EG Cnc and some other WZ Sge-type dwarf novae (Kato 2015), but later has also been invoked to interpret late superhumps and other peculiar properties of WZ Sge-type systems (Kato et al. 2008). It was shown that 'a cool matter reservoir' beyond the 3:1 resonance can supply the matter to the inner disc, resulting in rebrightenings, whereas the late superhumps should arise near the tidal truncation radius, from the matter in the reservoir.

In order to develop the model further it is essential to establish the time-scale of the reservoir filling and depleting. Our observations show that the Na D line has appeared in absorption no later than on $T = 28$, after that the line parameters were very stable until the end of the plateau stage. It suggests that the cool outer disc was already formed about three weeks after the beginning of the second segment of the superoutburst. However, the spectra obtained during the temporary fading stage between the superoutburst segments show the Na D line in emission. It implies that there was already a significant amount of matter in the reservoir at that time. Perhaps, the matter accumulated there during the first segment of the superoutburst. The following observations indicate that the reservoir depletion has been happening very slowly, because even 250 d after the superoutburst the system colours were redder than in quiescence, and also the late superhumps were observed at least 420 d after the superoutburst. Moreover, the sodium doublet was observed in emission until the most recent observations, obtained three years after the superoutburst. It has been steadily increasing the intensity in parallel with He I λ5876, suggesting a similar excitation mechanism of both lines.

Considering the very low mass ratio and also the long duration of the superoutburst, one can expect that a system similar to SSS J122222 can accumulate a significant amount of matter in the outer disc. It then seems to take years to drain this reservoir.

6.4 SSS J122222 as a period bouncer

The orbital period of SSS J122222, 109.80 min, is one of the longest among the WZ Sge-type stars (Kato 2015). In Section 5.2 we showed that at orbital periods of ∼2 h a contribution of the normal donor star to the NIR segment of the spectrum should dominate in quiescence, but is seemingly entirely absent. It suggests that the donor star has a low temperature and very low luminosity, that is consistent with the low K_1 and with very small $q \lesssim 0.045$ estimated from the period of superhumps. With such a small mass ratio even if the WD was close to the Chandrasekhar limit the donor mass must be below the hydrogen-burning minimum mass limit of 0.075 $M_\odot$. This suggests that SSS J122222 might already be evolving away from the period minimum towards longer periods, having passed through it, with the donor now extremely dim. Using a reasonable range of system parameters adopted above ($q = 0.015$–0.045, $M_{wd} = 0.8$–1.0 $M_\odot$, $d = 275$ pc) and assuming that the NIR spectrum is dominated by the WD only and that the contribution from the accretion disc is completely negligible, the residual NIR light sets a conservative upper limit on the temperature of the donor star of ∼2000 K. Moreover, the donor temperature is possibly significantly lower, because the disc probably contributes at NIR wavelengths (Hoard et al. 2002).

The properties of SSS J122222 are very similar to those of GD 522, another very strong period-bounce candidate with relatively long P_{orb} of 103 min (Unda-Sanzana et al. 2008). However, the longer period of SSS J122222, together with its small period excess, suggests that it is by far the most evolved CV known to date. Assuming that the only angular momentum loss mechanism in period-bounce CVs is that due to gravitational radiation, the age of SSS J122222 should be older than ∼6 Gyr (Howell et al. 1997).

We should note, however, that there is a separate evolutionary channel leading to brown-dwarf donors in CVs directly from detached WD/brown-dwarf binaries. Politano (2004) found, through population synthesis, that 18 per cent of the total zero-age CVs population are born with brown-dwarf donors, and 20 per cent of which have orbital periods in the range 78 to 150 min. The probability of finding that sort of system is not very high, though. According to the standard model of CV secular evolution, it is at least four times more likely that the donors in period-bounce candidates became substellar as a result of mass loss during secular evolution rather than that they were born substellar (Politano 2004). Moreover, the predicted distribution of orbital periods in CVs with the donors which were born substellar (fig. 2 in Politano 2004) shows a rapidly dwindling number of such CVs at longer P_{orb} (as in SSS J122222 and GD 522). Still, this alternative evolutionary scenario is possible.

Which evolutionary channel produced SSS J122222 and other period-bounce candidates can potentially be distinguished by the properties of the donor star. Since the donors in period bouncers were born as normal stars and became substellar during secular evolution, it is not obvious that these objects behave like ordinary brown dwarfs. In particular, the former objects should have comparatively higher helium abundance in comparison with normal brown dwarfs. Also, brown dwarfs (at least of a lower mass) do not burn lithium, whereas normal stars do, thus the lithium test (see e.g. Martin, Rebolo & Magazzu 1994) can be applied to distinguish brown dwarfs from substellar objects in period bouncers. Unfortunately, an accurate derivation of the helium abundance has proved difficult to perform even for normal stars, whereas even the strongest Li I λ6708 line is very weak and superposed on the broad and relatively strong He I λ6678 line. Therefore, we have to agree with Politano (2004) here that at the present time we cannot unambiguously

discriminate between brown dwarfs and substellar objects which were born as normal stars and became substellar as a result of mass loss.

7 SUMMARY

We have reported extensive UV–optical–NIR photometric and spectroscopic observations of the WZ Sge-type dwarf nova SSS J122222 during its superoutburst, the following decline and in quiescence. The observations were taken over three years, starting from 2013 January 5 (four days after the object's discovery) until 2016 April 17. The principal results of this study can be summarized as follows.

(i) The superoutburst showed two segments with an ∼5 mag and ∼10 d dip between them. The second segment had a long duration of 33 d and a very gentle decline with a rate of 0.02 mag d^{-1}.

(ii) The total amplitude of the superoutburst was ∼7 mag, and the post-outburst decline lasted no less than 500 d.

(iii) Superhumps with the average period of $P_{sh} = 110.23(7)$ min were clearly visible from our very first time-resolved observations until at least 420 d after the rapid fading from the superoutburst plateau. Thus, the late superhumps in SSS J122222 were detectable for a much longer time than in any other WZ Sge-type system. As in most SU UMa stars, P_{sh} in SSS J122222 changed slightly during the superoutburst and the following decline.

(iv) Multicolour photometry showed redder colours of superhumps at their light maximum, although the character of colour evolution of superhumps has also changed at different superoutburst stages.

(v) Simultaneously with the start of the decline, SSS J122222 showed the appearance of a strong NIR excess resulting in very red colours, which reached the extreme values ($B - I \simeq 1.4$) about 20 d later. The colours then became bluer again, but it took at least 250 d to acquire a stable level. We interpreted it as the appearance of a massive cool gas region in the outermost part of the disc, beyond the 3:1 resonance radius.

(vi) After the disappearance of the NIR excess, the observed IR flux of SSS J122222 in quiescence was much lower (7–10 times in the *JHKs* bands) than is expected from a CV with a near-main-sequence donor.

(vii) A time series analysis of the spectral data revealed an orbital period of 109.80(7) min. Thus, the fractional superhump period excess is $\lesssim$0.8 per cent, indicating a very low mass ratio $q \lesssim 0.045$. This is consistent with the low radial velocity semi-amplitude of the accretion disc emission lines, $K_1 = 16 \pm 5$ km s^{-1}.

(viii) A small q, very low luminosity and the lack of spectral signatures of the donor star strongly suggest its brown-dwarf-like nature and that SSS J122222 has already evolved away from the period minimum towards longer periods, although the scenario with the donor star that has not become substellar as a result of mass loss, but was born substellar cannot be ruled out.

(ix) A conservative upper limit on the temperature of the donor star is estimated to be 2000 K.

(x) The long orbital period suggests that SSS J122222 is by far the most evolved CV known to date.

ACKNOWLEDGEMENTS

TRM and DS are supported by the STFC under grant ST/L000733. KLP and JPO acknowledge the support of the UK Space Agency. SGP acknowledges financial support from FONDECYT in the form of grant number 3140585. GT and SVZ acknowledge PAPIIT grants IN-108316/IN-100614 and CONACyT grants 166376, 151858 and CAR 208512 for resources provided towards this research. VS thanks Deutsche Forschungsgemeinschaft (DFG) for financial support (grant WE 1312/48-1). This publication makes use of data products from the Wide-field Infrared Survey Explorer, which is a joint project of the University of California, Los Angeles, and the Jet Propulsion Laboratory/California Institute of Technology, funded by the National Aeronautics and Space Administration. We acknowledge the use of observations made with the NASA Galaxy Evolution Explorer. *GALEX* is operated for NASA by the California Institute of Technology under NASA contract NAS5-98034. We acknowledge with thanks the variable star observations from the AAVSO International Database contributed by observers worldwide and used in this research. The results presented in this paper are based on observations collected at the European Southern Observatory under programme IDs 290.D-5192 and 095.D-0837. We are thankful to the anonymous referee whose comments helped greatly to improve the paper.

REFERENCES

Araujo-Betancor S. et al., 2005, A&A, 430, 629
Aviles A. et al., 2010, ApJ, 711, 389
Berry R., Burnell J., 2005, The Handbook of Astronomical Image Processing, 2nd edn. Willmann-Bell, Richmond, VA
Burrows D. N. et al., 2005, Space Sci. Rev., 120, 165
Cannizzo J. K., 1993, ApJ, 419, 318
Cannizzo J. K., Still M. D., Howell S. B., Wood M. A., Smale A. P., 2010, ApJ, 725, 1393
Cannizzo J. K., Smale A. P., Wood M. A., Still M. D., Howell S. B., 2012, ApJ, 747, 117
Ciardi D. R., Howell S. B., Hauschildt P. H., Allard F., 1998, ApJ, 504, 450
Cutri R. M. et al., 2003, VizieR Online Data Catalog, 2246
D'Odorico S. et al., 2006, in McLean I. S., Iye M., eds, Proc. SPIE Conf. Ser. Vol. 6269, Ground-based and Airborne Instrumentation for Astronomy. SPIE, Bellingham, p. 626933
Drake A. J. et al., 2009, ApJ, 696, 870
Drake A. J. et al., 2013, Astron. Telegram, 4699, 1
Echevarria J., 1984, Rev. Mex. Astron. Astrofis., 9, 99
Echevarria J., Jones D. H. P., 1984, MNRAS, 206, 919
Gänsicke B. T. et al., 2009, MNRAS, 397, 2170
Gehrels N. et al., 2004, ApJ, 611, 1005
Hamilton R. T., Harrison T. E., Tappert C., Howell S. B., 2011, ApJ, 728, 16
Harrison T. E., 2016, ApJ, 816, 4
Harrison T. E., Hamilton R. T., Tappert C., Hoffman D. I., Campbell R. K., 2013, AJ, 145, 19
Hassall B. J. M., 1985, MNRAS, 216, 335
Hellier C., 2001, PASP, 113, 469
Hirose M., Osaki Y., 1990, PASJ, 42, 135
Hoard D. W., Wachter S., Clark L. L., Bowers T. P., 2002, ApJ, 565, 511
Howell S. B., Rappaport S., Politano M., 1997, MNRAS, 287, 929
Howell S. B., Hoard D. W., Brinkworth C., Kafka S., Walentosky M. J., Walter F. M., Rector T. A., 2008, ApJ, 685, 418
Ishioka R., Sekiguchi K., Maehara H., 2007, PASJ, 59, 929
Isogai M., Arai A., Yonehara A., Kawakita H., Uemura M., Nogami D., 2015, PASJ, 67, 7
Kato T., 2015, PASJ, 67, 108
Kato T., Maehara H., Monard B., 2008, PASJ, 60, L23
Kato T. et al., 2009, PASJ, 61, 395
Kato T., Maehara H., Uemura M., 2012, PASJ, 64, 63
Kato T., Monard B., Hambsch F.-J., Kiyota S., Maehara H., 2013, PASJ, 65, L11
Kato T. et al., 2014, PASJ, 66, 30
Kelson D. D., 2003, PASP, 115, 688
Kimura M. et al., 2016, PASJ, 68, 55
Knigge C., 2006, MNRAS, 373, 484

Knigge C., Baraffe I., Patterson J., 2011, ApJS, 194, 28
Kolb U., 1993, A&A, 271, 149
Kuulkers E., 2001, Astron. Nachr., 322, 9
Kuulkers E., Page K. L., Knigge C., Marsh T. R., Osborne J. P., Sivakoff G. R., 2013, Astron. Telegram, 4716, 1
Landolt A. U., 1992, AJ, 104, 340
Lasota J.-P., 2001, New Astron. Rev., 45, 449
Levato H. et al., 2013, Astron. Telegram 4700
Levine S., Chakrabarty D., 1995, IA-UNAM Technical Report MU-94-04
Mainzer A. et al., 2011, ApJ, 731, 53
Marino B. F., Walker W. S. G., 1979, in Bateson F. M., Smak J., Urch J. H., eds, IAU Colloq. 46, Changing Trends in Variable Star Research. Univ. Waikato, Hamilton, NZ, p. 29
Marsh T. R., 1989, PASP, 101, 1032
Marsh T., Knigge C., Pretorius R., Miller-Jones J., Koerding E., Sivakoff G., Woudt P., Warner B., 2013, ATel, 4704, 1
Marshall J. L. et al., 2008, in McLean I. S., Casali M. M., eds, Proc. SPIE Conf. Ser. Vol. 7014, Ground-based and Airborne Instrumentation for Astronomy II. SPIE, Bellingham, p. 701454
Martin E. L., Rebolo R., Magazzu A., 1994, ApJ, 436, 262
Mennickent R. E., Diaz M. P., 2002, MNRAS, 336, 767
Mennickent R. E., Sterken C., Gieren W., Unda E., 1999, A&A, 352, 239
Nagayama T. et al., 2003, in Iye M., Moorwood A. F. M., eds, Proc. SPIE Conf. Ser. Vol. 4841, Instrument Design and Performance for Optical/Infrared Ground-based Telescopes. SPIE, Bellingham, p. 459
Neustroev V. V., 2002, A&A, 382, 974
Neustroev V., Sjoberg G., 2013, Astron. Telegram, 4744, 1
Neustroev V. V., Zharikov S., Michel R., 2006, MNRAS, 369, 369
Neustroev V. V., Tovmassian G. H., Zharikov S. V., Sjoberg G., 2013, MNRAS, 432, 2596
Neustroev V. V., Zharikov S. V., Borisov N. V., 2016, A&A, 586, A10
Nogami D., Iijima T., 2004, PASJ, 56, 163
Nogami D. et al., 2009, ASP Conf. Ser. Vol. 404, Spectroscopic Observations of WZ Sge-type Dwarf Novae, GW Lib and V455 And in Superoutburst. Astron. Soc. Pac., San Francisco, p. 52
Oke J. B., 1990, AJ, 99, 1621
Osaki Y., 1989, PASJ, 41, 1005
Osaki Y., 1996, PASP, 108, 39
Osaki Y., Kato T., 2013, PASJ, 65
Patterson J., 2011, MNRAS, 411, 2695
Patterson J., Jablonski F., Koen C., O'Donoghue D., Skillman D. R., 1995, PASP, 107, 1183
Patterson J. et al., 1998, PASP, 110, 1290
Patterson J. et al., 2005, PASP, 117, 1204
Politano M., 2004, ApJ, 604, 817
Reichart D. et al., 2005, Nuovo Cimento C, 28, 767
Roming P. W. A. et al., 2005, Space Sci. Rev., 120, 95
Schneider D. P., Young P., 1980, ApJ, 238, 946
Schoembs R., Vogt N., 1980, A&A, 91, 25
Shafter A. W., Szkody P., Thorstensen J. R., 1986, ApJ, 308, 765
Still M., Howell S. B., Wood M. A., Cannizzo J. K., Smale A. P., 2010, ApJ, 717, L113
Tovmassian G., Zharikov S., 2013, Proc. IAU Sypm. Vol., 290, Feeding Compact Objects: Accretion on All Scales, p. 149
Tovmassian G. et al., 2003, PASP, 115, 725
Tovmassian G. H., Zharikov S. V., Neustroev V. V., 2007, ApJ, 655, 466
Uemura M., Kato T., Ohshima T., Maehara H., 2012, PASJ, 64
Unda-Sanzana E. et al., 2008, MNRAS, 388, 889
van Spaandonk L., Steeghs D., Marsh T. R., Torres M. A. P., 2010, MNRAS, 401, 1857
Verbunt F., 1987, A&AS, 71, 339
Vican L. et al., 2011, PASP, 123, 1156
Vogt N., 1982, ApJ, 252, 653
Vogt N., 1983, A&A, 118, 95
Warner B., 1995, Cataclysmic Variable Stars. Cambridge Astrophysics Ser. 28; Cambridge Univ. Press, Cambridge
Whitehurst R., 1988, MNRAS, 232, 35
Wood M. A., Still M. D., Howell S. B., Cannizzo J. K., Smale A. P., 2011, ApJ, 741, 105
Wu C.-C., Panek R. J., 1983, ApJ, 271, 754
Zharikov S. V., Tovmassian G. H., Napiwotzki R., Michel R., Neustroev V., 2006, A&A, 449, 645

APPENDIX A: OBSERVATIONS AND DATA REDUCTION

A1 Optical photometric observations

Most of the optical time-resolved photometric observations were taken by three observatories located in Chile and New Mexico. The ROAD in Chile houses a 0.40-m f/6.8 ODK telescope from Orion Optics UK, equipped with a CCD camera from Finger Lakes Instrumentation, an FLI ML16803 CCD, which holds a Kodak KAF-16803 CCD chip with 4k × 4k pixels. All the measurements made with this telescope between 2013 January 8 and 2013 March 15 were unfiltered (the CCD response is close to that of the *V* filter). The exposure times were 60 s during the outburst stage, but were increased to 120 s when the source faded. Some of these data were already presented by Kato et al. (2013). The observations at New Mexico Skies in Mayhill, New Mexico, were performed from 2013 January 11 to 2013 February 26 with the 0.35-m Celestron C14 robotic telescope and an SBIG ST-10XME CCD camera with Johnson–Cousins $BV(RI)_C$ Astrodon Photometric filters. The images were usually taken in a sequence *B*–*V*–*R*–*I*. During the bright state the exposure times were 15 s for the *VRI* filters and 30 s for *B*. They were increased to 240 and 400 s, respectively, when the source declined in brightness. Depending on the weather conditions, we monitored the star for 4–8 h per night. Since 2013 March 5, we started using two 0.4-m robotic PROMPT telescopes located in Chile (Reichart et al. 2005). After 2013 March 17, only the PROMPT telescopes were utilized. Most of the PROMPT observations in 2013 were performed in the *V* filter, whereas the data obtained in 2014 and 2015 are mostly unfiltered (the CCD response is close to that of the *R* filter) though occasionally we also took $BV(RI)_C$ data. The exposure times were 180 s. In addition, during 2013 February 5–7 we obtained three nights of time-resolved observations with the 0.84 m telescope at the Observatorio Astronómico Nacional at San Pedro Mártir (OAN SPM) in Mexico. These observations in the Johnson *V* filter were performed with exposure times of 30 s, simultaneously with the spectroscopic observations at the same site (see Section A4).

In order to establish the zero-points and calibrate the comparison stars, on 2013 February 5 we obtained $UBV(RI)_C$ images of eight Landolt standards (Landolt 1992). These standards were observed several times at different airmasses throughout the night. The comparison stars which were checked for variability are indicated in Fig. A1, and their corresponding magnitudes are listed in Table A1. The errors are formal 1-σ uncertainties returned by the fit and are likely to underestimate the real uncertainties.

The data reduction was performed using the IRAF environment and the software AIP4Win v. 2.4.0 (Berry & Burnell 2005). All images were corrected for bias and flat-fielded in the standard way. We performed aperture photometry of our object and several comparison stars. Reducing the unfiltered observations, we used the *V* and *R* comparison star magnitudes for the ROAD and PROMPT data, respectively. Our tests showed that such an approach could induce measurement errors no more than a few hundredth of magnitude, in comparison with filtered photometry. The typical accuracy of source measurements during the bright state was about 0.02–0.03 mag,

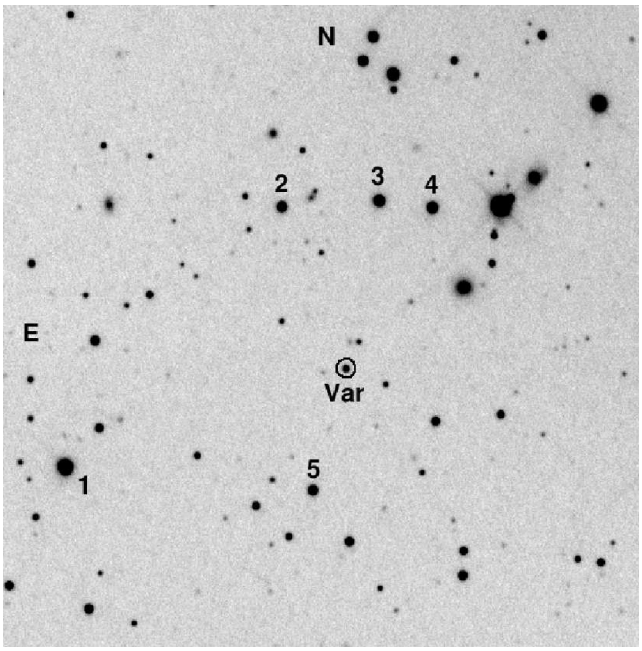

Figure A1. The 6 × 6 arcmin^2 field of view of SSS J122222, oriented such that up is North and left is East. The object's location is indicated by a ring. Calibrated comparison stars are labelled as 1, 2, 3, 4 and 5, and their magnitudes are listed in Table A1.

which then worsened to 0.05–0.15 mag when the source declined in brightness.

In order to simplify the analysis of the long-term light curve, we also formed 1-d averages of all the observations, reducing thus the scatter from both random errors and stochastic and short-term variability. On average, each night of observations during the bright state contains about 68 *V*-band and/or unfiltered data points and 55 data points in the *B*, *R* and *I* bands. Post-outburst nightly observations consist on average of 14, 52, 36 and 14 exposures in the *B*, *V*, *R* (including unfiltered) and *I* filters. The median values of the standard error of these 1-d averages are better than 0.01 and 0.05 mag in all the filters for the bright-state and post-outburst observations, respectively. We also note that the *BVRI* images obtained in 2014, 2015 and 2016 are rather noisy. In order to improve the confidence of the colour measurements we first aligned and summed all the nightly images for each filter and then measured the average magnitudes.

Table A2 provides the journal of the optical time-resolved photometric observations. In order to help the reader to trace long-term brightness evolution of SSS J122222, we also show its 1-d averaged *V* magnitudes. For the nights when no data in this filter were taken, the *V* magnitudes were obtained from the *R* magnitudes and *V*–*R* colour indices interpolated to the night in question.

A2 NIR observations

A near-infrared observation of SSS J122222 was conducted on 2016 April 7 using the IRSF at Sutherland, South Africa. The IRSF consists of a 1.4 m telescope and SIRIUS (Nagayama et al. 2003). The SIRIUS camera can obtain *J*, *H* and *Ks* band images simultaneously, with three 1K × 1K HgCdTe detectors. It has a square field of view of 7.7 × 7.7 arcmin^2 and a 0.45 arcsec pixel^{-1} pixel scale. During our observations, the exposure time of a frame was 60 s and a total of 130 frames with 10-point dithering were taken during 150 min. Data reduction was carried out with a pipeline for SIRIUS,[10] which includes a correction for non-linearity, dark subtraction, and flat-fielding. The IR magnitudes were calibrated using the same comparison stars as were chosen for the optical photometry (Fig. A1, Table A1). Their magnitudes and errors were taken from the 2MASS All-Sky Catalogue of Point Sources (Cutri et al. 2003).

A3 *Swift* UVOT observations

The *Swift* X-ray satellite (Gehrels et al. 2004) started observing SSS J122222 on 2013 January 6. Data were collected using both the XRT telescope and the UVOT with the *uvm*2 filter in position. Following the initial 4 ks exposure, 1–2 ks observations were obtained approximately every 1–3 d until 2013 July 1, with occasional gaps in the schedule caused by high priority *Swift* observations of other targets. On 2014 June 26 and on 2015 January 16 we performed two additional observations. A final data set was collected on 2016 April 17. This UVOT observation was carried out in all six filters: *uvw*2 (central wavelength 1928 Å), *uvm*2 (2246 Å), *uvw*1 (2600 Å), *u* (3465 Å), *b* (4392 Å) and *v* (5468 Å).

The data were processed and analysed using HEASOFT 6.16, together with the most recent version of the calibration files. The UVOT magnitudes were calculated using a standard 5 arcsec extraction region, with the background estimated from four nearby circular source-free regions. Table A3 gives details of the *Swift* observations.

A4 Spectroscopic observations

Table A4 provides the journal of the optical spectroscopic observations. The first two sets of spectroscopic data were obtained at the end of the nights starting 2013 January 4 and 5 with the 4.2-m William Herschel Telescope on La Palma. The observations were taken with the dual arm spectrograph ISIS, using the 600 lines/mm gratings in the blue and red arms to cover the wavelength intervals 3945–5170 Å at 0.88 Å pixel^{-1} and 5614–7140 Å at 0.98 Å pixel^{-1}, respectively; the FWHM resolution in each arm was 2.0 Å. The total exposure times were 29 and 92 min, respectively, with the majority of exposure 5 min in duration. We used a slit width of 1.2 arcsec. The weather was clear on both nights, and the seeing was around ∼1.2 arcsec on the second night, however the southerly position of SSS J122222, meaning that all data were acquired at high airmass, which, along with poor seeing on the first night, cost significant throughput; given the narrow slit, no flux calibration was attempted. The observations were reduced using the STARLINK software packages FIGARO, KAPPA and PAMELA to extract the spectra optimally (Marsh 1989). The wavelength scales were linearly interpolated in time from bracketing comparison arc spectra. We fitted 30 and 28 lines with cubic polynomials (four coefficients) obtaining rms scatters of 0.015 and 0.021Å in the blue and red arms, respectively.

Twelve observations were obtained at the OAN SPM in Mexico on the 2.1-m telescope. The data on 2013 January 28 were obtained with the Echelle spectrograph (Levine & Chakrabarty 1995). This instrument gives a resolution of 0.234 Å pixel^{-1} at Hα using the UCL camera and a CCD-Tek chip of 1024 × 1024 pixels with a 24 μm^2 pixels size. The spectra cover 25 orders and span the spectral range 3915–7105 Å. A total of 12 spectra were obtained with

[10] http://irsf-software.appspot.com/yas/nakajima/sirius.html

Table A1. Magnitudes of comparison stars in the field of SSS J122222. The $UBV(RI)_C$ magnitudes and their errors were determined in this work, while the *JHKs* magnitudes were taken from the 2MASS All-Sky Catalogue of Point Sources (Cutri et al. 2003).

Star	U	B	V	R_c	I_c	J	H	Ks
1	15.07 ± 0.03	14.87 ± 0.02	14.14 ± 0.02	13.65 ± 0.02	13.19 ± 0.03	12.58 ± 0.02	12.15 ± 0.02	12.06 ± 0.02
2	16.63 ± 0.05	16.76 ± 0.03	16.28 ± 0.03	15.89 ± 0.03	15.43 ± 0.04	15.13 ± 0.06	14.86 ± 0.06	14.58 ± 0.09
3	14.69 ± 0.03	16.20 ± 0.02	15.65 ± 0.02	15.20 ± 0.02	14.80 ± 0.03	14.28 ± 0.03	13.94 ± 0.04	13.86 ± 0.06
4	16.55 ± 0.05	16.37 ± 0.02	15.77 ± 0.02	15.37 ± 0.02	14.98 ± 0.04	14.52 ± 0.03	14.30 ± 0.05	14.08 ± 0.07
5	17.73 ± 0.11	17.10 ± 0.04	16.41 ± 0.03	15.85 ± 0.03	15.28 ± 0.04	14.74 ± 0.04	14.22 ± 0.05	14.32 ± 0.07

Table A2. Journal of photometric observations of SSS J122222. The table also provides the 1-d averaged V magnitudes of the source (see text for details).

HJD start 245 0000+	Duration (h)	Band	V (mag)	HJD start 245 0000+	Duration (h)	Band	V (mag)	HJD start 245 0000+	Duration (h)	Band	V (mag)
6300.726	2.66	*V*	16.79	6356.589	5.19	*BVRI*	17.51	6461.574	0.63	*V*	18.38
6301.723	2.72	*V*	16.67	6357.622	5.87	*BVRI*	17.47	6509.502	1.21	*BVRI*	18.40
6303.735	2.42	*V*	14.43	6358.632	3.33	*V*	17.51	6670.658	0.70	*BVRI*	18.82
6304.006	0.17	*V*	13.74	6360.627	6.37	*BVRI*	17.70	6675.695	1.39	*R*	18.87
6304.715	2.93	*V*	12.60	6361.615	6.32	VRI	17.61	6676.666	4.22	*R*	18.86
6305.713	3.03	*V*	12.37	6362.633	3.79	*V*	17.65	6677.740	1.34	*R*	19.05
6306.772	1.63	*V*	12.20	6363.576	5.09	*V*	17.74	6686.735	2.65	*R*	18.85
6307.707	3.69	*V*	12.28	6364.550	5.64	*V*	17.62	6687.623	5.75	*R*	18.89
6308.772	6.45	*V*	12.55	6365.525	6.92	*V*	17.69	6688.620	3.92	*R*	18.91
6309.728	7.63	*BVRI*	12.58	6366.625	3.73	*V*	17.68	6699.591	4.30	*R*	18.94
6310.801	5.93	*BVRI*	12.46	6367.520	6.95	*V*	17.70	6708.695	4.45	*R*	18.94
6312.922	2.94	*BVRI*	12.31	6368.559	5.51	*V*	17.77	6709.568	4.54	*R*	18.91
6314.689	8.58	*BVRI*	12.39	6371.604	7.06	*BVRI*	17.83	6710.572	5.62	*R*	18.94
6315.917	3.06	*BVRI*	12.41	6372.708	3.19	*BVRI*	17.81	6711.608	5.68	*R*	18.87
6316.789	2.24	*V*	12.40	6377.630	6.11	*BVRI*	17.86	6712.616	0.15	*R*	18.87
6317.680	4.87	*V*	12.41	6378.559	4.34	*V*	17.87	6713.594	6.95	*R*	18.91
6318.678	4.96	*V*	12.41	6380.751	3.06	*V*	17.92	6714.711	4.20	*R*	18.82
6319.675	5.01	*V*	12.42	6383.512	4.13	*V*	18.01	6715.552	5.59	*R*	18.78
6320.673	4.61	*V*	12.44	6384.510	1.99	*V*	17.98	6716.659	2.80	*BVRI*	18.88
6321.719	4.01	*V*	12.48	6385.549	2.95	*V*	18.09	6717.745	3.42	*R*	18.75
6323.665	9.06	*BVRI*	12.52	6386.518	4.68	*V*	18.05	6719.539	3.15	*R*	18.77
6324.662	9.40	*BVRI*	12.56	6388.541	4.22	*V*	17.96	6720.535	2.73	*R*	18.80
6325.660	5.52	*V*	12.57	6389.507	5.23	*BVRI*	17.95	6721.565	3.66	*R*	18.69
6326.660	5.48	*V*	12.61	6393.596	5.56	*V*	18.03	6722.656	3.10	*BVRI*	18.86
6327.658	9.36	*BVRI*	12.65	6394.546	4.87	*V*	18.02	6723.534	2.17	*BVRI*	18.90
6328.890	3.71	*UBVRI*	12.69	6395.520	5.27	*BVRI*	18.05	6726.525	3.67	*R*	18.83
6329.888	4.07	*BVRI*	12.72	6397.515	4.29	*V*	18.07	6727.525	3.67	*R*	18.83
6330.873	4.04	*BVRI*	12.77	6398.512	4.21	*V*	18.07	6728.588	3.66	*R*	18.79
6331.883	3.85	*BVRI*	12.81	6401.729	3.52	*V*	18.00	6729.523	3.77	*R*	18.71
6334.861	4.03	*BVRI*	12.96	6402.501	0.52	*V*	18.13	6730.527	3.83	*R*	18.74
6336.625	9.74	*BVRI*	14.55	6403.712	3.78	*V*	18.10	6746.508	4.23	*R*	18.81
6337.729	7.35	*BVRI*	15.90	6416.726	2.59	*V*	18.12	6749.530	5.38	*R*	18.72
6338.624	6.38	*V*	16.16	6417.486	8.26	*V*	18.25	6750.609	3.72	*BVRI*	18.96
6339.645	9.34	*BVRI*	16.45	6418.487	7.77	*BVRI*	18.24	6752.503	4.40	*R*	18.85
6340.642	9.23	*BVRI*	16.65	6423.780	0.83	*V*	18.29	6755.519	4.31	*R*	18.86
6341.786	5.92	*BVRI*	16.75	6424.483	5.61	*V*	18.14	6772.558	3.72	*BVRI*	18.94
6342.637	9.31	*BVRI*	16.86	6427.481	7.33	*V*	18.22	6827.546	3.70	*BVRI*	19.01
6343.634	6.34	*V*	16.96	6428.480	7.67	*V*	18.11	6836.548	3.70	*BVRI*	18.96
6344.631	6.41	*V*	17.13	6431.538	5.47	*V*	18.25	7036.750	0.40	*R*	19.02
6345.778	5.87	*BVRI*	17.17	6432.478	4.85	*V*	18.29	7037.763	3.20	*BVRI*	19.02
6346.843	4.22	*V*	17.25	6433.479	4.66	*V*	18.33	7040.826	0.59	R	19.00
6347.679	5.28	*V*	17.28	6434.477	6.11	*V*	18.36	7041.809	1.01	R	18.95
6348.666	5.71	*V*	17.33	6436.476	5.32	*BVRI*	18.31	7043.645	2.67	R	19.10
6349.656	7.36	*V*	17.43	6442.540	0.51	*BVRI*	18.24	7060.599	2.56	R	18.88
6351.650	6.09	*V*	17.40	6446.474	4.72	*BVRI*	18.34	7061.627	1.29	R	18.71
6352.716	4.22	*V*	17.55	6448.476	6.43	*BVRI*	18.31	7062.594	3.16	R	19.01
6353.601	6.90	*BVRI*	17.40	6458.557	0.99	*BVRI*	18.41	7063.591	1.39	R	18.85
6354.596	7.06	*BVRI*	17.43	6459.633	0.21	*V*	18.43	7403.120	0.77	*BVRI*	19.03
6355.546	4.83	*V*	17.49	6460.588	2.73	*BVRI*	18.46	7497.323	3.12	*BVRI*	19.01

Table A3. Details of the *Swift* observations of SSS J122222.

HJD mid 245 0000+	Obs. ID	Exp. time (ksec)	*uvm2* (mag)	HJD mid 245 0000+	Obs. ID	Exp. time (ksec)	*uvm2* (mag)
6299.385	00032666001/1	1.92	14.83 ± 0.03	6348.749	00032666027	0.26	15.76 ± 0.05
6299.447	00032666001/2	2.04	14.80 ± 0.02	6349.397	00032666027	0.65	15.65 ± 0.03
6301.381	00032666002	1.98	–	6352.003	00032666028	1.04	15.99 ± 0.03
6303.115	00032666003/1	1.45	14.90 ± 0.03	6354.805	00032666029	0.95	15.81 ± 0.03
6303.199	00032666003/2	0.53	15.26 ± 0.03	6357.950	00032666030	0.94	15.74 ± 0.03
6305.329	00032666004/1	1.80	10.87 ± 0.02	6364.289	00032666032	0.99	15.83 ± 0.03
6305.395	00032666004/2	0.17	10.84 ± 0.03	6369.639	00032666034	1.00	16.06 ± 0.03
6307.199	00032666005	1.80	10.64 ± 0.02	6372.710	00032666035	1.06	15.97 ± 0.03
6309.406	00032666006/1	1.04	–	6376.443	00032666036	1.11	16.08 ± 0.03
6309.472	00032666006/2	0.91	–	6378.519	00032666037	1.13	16.01 ± 0.03
6310.997	00032666007/1	1.62	10.87 ± 0.02	6381.599	00032666038	0.90	16.05 ± 0.04
6311.391	00032666007/2	0.49	10.86 ± 0.02	6384.658	00032666039	1.02	16.21 ± 0.04
6313.198	00032666008/1	0.87	–	6387.530	00032666040	0.91	16.15 ± 0.04
6313.411	00032666008/2	1.22	–	6391.320	00032666041	1.02	16.20 ± 0.04
6315.071	00032666009/1	1.68	10.75 ± 0.02	6394.210	00032666042	0.94	16.27 ± 0.04
6315.133	00032666009/2	0.55	10.75 ± 0.02	6397.075	00032666043	0.91	16.23 ± 0.04
6317.004	00032666010/1	0.93	10.80 ± 0.02	6399.962	00032666044	0.99	16.26 ± 0.04
6317.071	00032666010/2	1.01	10.85 ± 0.02	6407.992	00032666046	1.03	16.28 ± 0.04
6318.944	00032666011/1	1.32	10.74 ± 0.02	6416.000	00032666047	1.05	16.37 ± 0.04
6319.007	00032666011/2	0.72	10.76 ± 0.02	6418.949	00032666048	0.96	16.40 ± 0.04
6322.354	00032666012	1.12	10.90 ± 0.02	6421.980	00032666049	1.02	16.41 ± 0.04
6324.555	00032666013	1.01	10.87 ± 0.02	6424.929	00032666050	0.76	16.45 ± 0.04
6327.706	00032666014	1.05	11.02 ± 0.02	6428.338	00032666051	1.02	16.41 ± 0.04
6330.836	00032666015	1.00	11.18 ± 0.02	6430.733	00032666052	0.99	16.51 ± 0.04
6333.839	00032666016	1.09	11.34 ± 0.02	6434.017	00032666053/1	0.82	16.37 ± 0.04
6337.197	00032666017	0.28	13.31 ± 0.03	6434.081	00032666053/2	0.19	16.53 ± 0.08
6338.122	00032666018	0.48	14.72 ± 0.03	6436.953	00032666054	1.09	16.52 ± 0.04
6338.385	00032666019	0.49	14.95 ± 0.03	6439.958	00032666055	1.06	16.60 ± 0.04
6338.647	00032666020	1.03	14.96 ± 0.03	6442.913	00032666056	0.86	16.44 ± 0.04
6339.385	00032666021	0.98	15.03 ± 0.03	6445.833	00032666057	0.86	16.58 ± 0.04
6339.918	00032666022	1.05	15.10 ± 0.03	6449.463	00032666058	0.46	16.56 ± 0.05
6340.450	00032666023	1.04	15.03 ± 0.03	6451.455	00032666059	0.73	16.54 ± 0.04
6341.850	00032666024/1	1.17	15.41 ± 0.03	6457.962	00032666060	1.03	16.60 ± 0.04
6341.919	00032666024/2	1.59	15.27 ± 0.03	6464.171	00032666062	1.04	16.63 ± 0.14
6341.986	00032666024/3	2.00	15.37 ± 0.03	6467.190	00032666063	1.04	16.26 ± 0.04
6342.045	00032666024/4	0.20	15.46 ± 0.05	6475.068	00032666065	1.04	16.54 ± 0.04
6342.927	00032666025/1	0.60	15.51 ± 0.03	6835.086	00032666066	2.95	17.52 ± 0.04
6342.983	00032666025/2	0.60	15.29 ± 0.03	7038.833	00032666068	1.91	17.63 ± 0.09
6345.652	00032666026/1	0.21	15.49 ± 0.05	7496.135	00032666069	2.06	17.53 ± 0.09
6345.930	00032666026/2	0.99	15.58 ± 0.03				

Note. The Obs. ID is a unique identifier given to every observation taken with *Swift*. The Obs. ID column also shows the snapshot number after the slash; a snapshot is a time interval spent continuously observing the same sky position. The *uvm2* column indicates the measured *uvm2* magnitude of SSS J122222 during the corresponding snapshot.

600 s individual exposures. The reduction procedure was performed using IRAF. Comparison spectra of Th–Ar lamps were used for the wavelength calibration. The absolute flux calibration of the spectra was achieved by taking nightly echellograms of the standard stars HD93521 and HR153. Further observations with this telescope were conducted on 2013 February 5–8, on February 10–13, on May 5 and on 2016 February 9 and 10 with the Boller and Chivens (B&Ch) spectrograph, equipped with a 13.5 μm (2174 × 2048) Marconi E2V-4240 CCD chip. Spectra were obtained in both single-shot and time-resolved manner with different instrumental setups and exposure times. For details see Table A4. Several Cu–He–Ne–Ar lamp exposures were taken during the observations of the target for wavelength calibrations, and the standard spectrophotometric stars Feige 110, HR3454 and G191-B2B (Oke 1990) were observed for flux calibrations. The data reduction was also performed using the IRAF environment. All the nights of the observations at OAN SPM were photometric with exception for the first half of the night of 2013 February 6 when a part of the output spectra was ruined by clouds. An unaffected subset of this night's data includes five spectra taken in the beginning and 30 spectra obtained in the end of the observations, with a total exposure time of 103 min.

Another set of spectroscopic data was taken with the MagE spectrograph (Marshall et al. 2008) on the Magellan Clay Telescope on 2013 February 5. These observations were gathered on the same night as one of the OAN SPM observations, but they do not overlap. The object was observed with the 1.0 arcsec slit, for a total of 91 min, broken up into 22 blocks of 300–600 s, separated by Th–Ar lamp measurements. Seeing varied from 0.9 to 1.5 arcsec over the course of the observations. The standard spectrophotometric star Feige 67 was observed with the same setup. So were various calibration frames such as Xe-flash frames, quartz lamp frames and Th–Ar frames from flat-fielding and wavelength calibration purposes. Data were reduced with the Carnegie MagE pipeline (first described in Kelson 2003). The orders of the combined spectrum were

Table A4. Log of spectroscopic observations of SSS J122222.

HJD start 245 0000+	Telescope/ instrument	λ range (Å)	Exp. time (s)	Number of exp.	Duration (h)	Magnitude (*V*)
6297.765	WHT/ISIS	3915–7105	600	5	2.00	16.0
6298.741	WHT/ISIS	3915–7105	600	13	2.00	16.4
6320.942	2.1 m/Echelle	3775–7350	600	12	2.11	12.4
6328.832	Magellan/MagE	3040–8280	180–300	22	1.52	12.7
6328.894	2.1 m/B&Ch	3775–7275	180	60	3.48	12.7
6329.893	2.1 m/B&Ch	3775–7275	180	44	3.37	12.7
6330.946	2.1 m/B&Ch	4555–6930	300	38	2.06	12.8
6331.880	2.1 m/B&Ch	3720–7220	300	1	0.08	12.8
6333.871	2.1 m/B&Ch	3720–7220	300	1	0.08	12.9
6334.872	2.1 m/B&Ch	3720–7220	300	1	0.08	13.0
6335.984	2.1 m/B&Ch	4465–5685	600	12	1.90	13.5
6336.902	2.1 m/B&Ch	5700–6820	600	18	3.66	14.6
6372.715	VLT/X-Shooter	3000–24760	130–160	36	1.89	17.8
6417.697	2.1 m/B&Ch	3780–6145	600	12	1.89	18.2
7148.483	VLT/FORS2	3830–10100	300	4	0.46	19.0
7427.959	2.1 m/B&Ch	4330–6700	1200	3	1.01	19.0
7428.933	2.1 m/B&Ch	4330–6700	600	13	2.24	19.0

Note. The Magnitude column indicates the approximate magnitude of SSS J122222 during the observation. They are taken from simultaneous or interpolated from recent photometric observations.

normalized and merged to produce final one-dimensional spectra for further analysis.

On 2013 March 21 SSS J122222 was observed with the medium-resolution spectrograph X-shooter (D'Odorico et al. 2006) mounted at the Cassegrain focus of VLT-UT2 at Paranal. X-shooter comprised three detectors: the UVB arm, which gives spectra from 0.3 to 0.56 μm, the VIS arm which covers 0.56–1 μm and the NIR arm which covers 1–2.4 μm. We used slit widths of 1.0 arcsec, 0.9 arcsec and 0.9 arcsec in X-shooter's three arms and 2–×–2 binning in the UVB and VIS arms resulting in a spectral resolution of 3000–4000 across the entire spectral range. The reduction of the raw frames was conducted using the standard pipeline release of the X-shooter Common Pipeline Library (CPL) recipes (version 6.5.1) within ESORex, the ESO Recipe Execution Tool, version 3.11.1. The standard recipes were used to optimally extract and wavelength calibrate each spectrum. The instrumental response was removed by observing the spectrophotometric standard star EG274 and dividing it by a flux table of the same star to produce the response function. The wavelength scale was also heliocentrically corrected. During our observations we nodded the object along the slit in order to improve the NIR arm reduction. However, we decided to reduce the data in STARE mode to increase the phase resolution of the data. While this had no effect on the UVB and VIS arm reductions, the sky subtraction was poorer in the NIR arm using this method; nevertheless, the improved phase resolution gained by this method outweighed the poorer sky subtraction.

On 2015 May 5 we performed the observations with the FORS2 spectrograph mounted at the Cassegrain focus of VLT-UT1 at Paranal. In order to maximize the wavelength coverage, we took two spectra using the GRIS_300V+10 grism and two using the GRIS_300I+11 grism, providing an overall wavelength coverage of 3830–10110 Å. The exposure times were 300 s. We used a 1 arcsec slit and 2–×–2 binning of the MIT CCD, resulting in a resolution of 12 Å at the central wavelength. The spectra were reduced using KAPPA, FIGARO and PAMELA. The wavelength scale was derived from Hg–Cd and He–Ne–Ar arc lamp exposures taken in the morning following the observations, with the telescope pointing at zenith. To account for any flexure, we adjusted the wavelength scale using the known wavelengths of strong night-sky lines. Although the sky was clear at the time of the target observations, the morning twilight was cloudy, so no spectroscopic flux standard was taken. Instead, we used archival spectra of LTT3864, taken with the same instrument setup, to derive an approximate flux calibration.

This paper has been typeset from a TEX/LATEX file prepared by the author.